Stem cells tightly regulate dead cell clearance to maintain tissue fitness

Katherine S Stewart[1], Kevin AU Gonzales[1†], Shaopeng Yuan[1], Matthew T Tierney[1], Alain R Bonny[1], Yihao Yang[1], Nicole R Infarinato[1†], Christopher J Cowley[1], John M Levorse[1†], Hilda Amalia Pasolli[2], Sourav Ghosh[3], Carla V Rothlin[4], & Elaine Fuchs[1, ‡]

Affiliations

[1]Howard Hughes Medical Institute, Robin Chemers Neustein Laboratory of Mammalian Cell Biology and Development, The Rockefeller University, New York, NY, USA

[2]Electron Microscopy Resource Center, The Rockefeller University, New York, NY, USA

[3]Departments of Neurology and Pharmacology, Yale School of Medicine, New Haven, CT, USA

[4]Departments of Immunobiology and Pharmacology, Yale School of Medicine, New Haven, CT, USA

‡For reagents and queries, contact: fuchslb@rockefeller.edu
Corresponding author with the editor, email: fuchs@rockefeller.edu

† *Present Addresses:* Department of Discovery Technology and Genomics, Novo Nordisk Research Centre Oxford, Oxford, UK (K.A.G); PrecisionScienta, Yardley, PA, USA (N.I.); Cardiovascular Research Group, Temple University, Philadelphia, PA, USA (J.L.)

Summary Paragraph

Macrophages and dendritic cells have long been appreciated for their ability to migrate to and engulf dying cells and debris, including some of the billions of cells that are naturally eliminated from our body daily. However, a substantial number of these dying cells are cleared by 'non-professional phagocytes', local epithelial cells that are critical to organismal fitness. How non-professional phagocytes sense and digest nearby apoptotic corpses while still performing their normal tissue functions is unclear. Here, we explore the molecular mechanisms underlying their multifunctionality. Exploiting the cyclical bouts of tissue regeneration and degeneration during the hair cycle, we show that stem cells can transiently become non-professional phagocytes when confronted with dying cells. Adoption of this phagocytic state requires both local lipids produced by apoptotic corpses to activate RXRα, and tissue-specific retinoids for RARγ activation. This dual factor dependency enables tight regulation of the genes requisite to activate phagocytic apoptotic clearance. The tunable phagocytic program we describe here offers an effective mechanism to offset phagocytic duties against the primary stem cell function of replenishing differentiated cells to preserve tissue integrity during homeostasis. Our findings have broad implications for other non-motile stem or progenitor cells which experience cell death in an immune-privileged niche.

Main

Adult homeostatic tissue maintenance necessitates the turnover and replacement of billions of cells daily [1,2]. Tissue rejuvenation is achieved by stem cells, which balance proliferation and differentiation through carefully charted programs. However, when cells within a tissue die, they must be removed quickly to maintain immune and tissue homeostasis. Clearance of apoptotic cells ('efferocytosis') is the provenance of both professional (immune cells) and non-professional (epithelial and mesenchymal cells) phagocytes[2-5]. In developmental, homeostatic, and pathological contexts, phagocytic cells detect and engulf apoptotic corpses. Failure to do so results in secondary necrosis, which can result in many inflammatory and/or degenerative pathologies[1,6-8].

Dead cell clearance is a step-wise process initiated when apoptotic corpses transmit "find-me" signals, which are then recognized by clearance receptors on phagocytic cells[2-6]. The sensing mechanisms have been well-described for motile professional phagocytes, such as macrophages and dendritic cells, which are defined by their constitutive phagocytic functions, but remain less clear for non-motile non-professional phagocytes[4]. Nonetheless, engagement of clearance receptors in most if not all phagocytes converges on downstream activation of the Elmo-Dock-Rac pathway to mediate actin cytoskeleton rearrangement and facilitate uptake of apoptotic bodies[2-6]. Subsequent digestion of apoptotic corpses occurs via phagosome maturation and fusion with lysosomes, wherein corpse-derived materials are degraded[2-6,9].

How non-motile, non-professional phagocytes regulate apoptotic cell clearance in tissues remains unclear. The issue is an important one as in contrast to their immune counterparts, non-professional phagocytes have other dedicated roles in tissue function. We hypothesize that they are able to transiently and expeditiously activate phagocytosis and then dial it down again to return to their normal tissue tasks. Here, we explore this in the context of a dynamic tissue setting by focusing on the synchronized hair cycles of regenerative growth (anagen), degeneration (catagen), and quiescence (telogen) (**Fig. 1a**).

The hair follicle stem cells (HFSCs) that fuel this cycle reside in a niche ('bulge') within the HF. During the early growth phase, they proliferate to generate the outer root sheath (ORS) and the differentiating hair lineages encased therein. The upper ORS becomes quiescent early, setting aside stem and progenitor cells to form a new bulge for the next hair cycle, while the lower ORS contain short-lived progeny that contribute to hair growth.[10,11,12] During catagen, terminal differentiation of the hair lineages and apoptosis within the ORS[13] converge with contractile forces from the surrounding dermal sheath[14] to drive HF involution. Notably, during the regressive phase, apoptotic cells in the lower ORS are cleared by neighbouring epithelial cells[13,15], but how this occurs remains unclear.

Hair follicle stem and progenitor cells engulf corpses during physiological apoptosis

To elucidate the spatiotemporal pattern of apoptotic cell clearance across the hair cycle, we used immunofluorescence microscopy to identify dying cells, which are positive for cleaved caspase-3 (Casp3^{+}) and DNA damage (terminal-uridine-nick-end-labelling, TUNEL[+]), and monitored their engulfment (TUNEL[+] apoptotic body inside a healthy P-cadherin[+] ORS cell with a normal nucleus) (**Fig. 1b**). Dying HF cell

2

80   numbers increased progressively throughout the catagen ORS. As previously reported, apoptotic cell death

81   was high in the lower ORS.[6,9,12] That said, apoptotic cells were also found within the upper ORS, previously

82   assumed to be unaffected[10,13].

83   In agreement with a prior report[13], CD45+ professional phagocytes showed no signs of phagocytic

84   activity at this time (**Extended data Fig. 1a**). By contrast, healthy basal ORS epithelial progenitors displayed

85   numerous TUNEL[+] condensed apoptotic bodies within their cytoplasm, indicative of phagocytosis (**Fig. 1b**).

86   The timing and patterning of phagocytic cells paralleled that of dying cells. Phagocytic HF cells were in equal

87   proportion to apoptotic cells early in catagen (CatII) but increased to roughly twice as many by late catagen

88   (**Extended data Fig. 1b**). Notably, at the end of catagen, engulfed apoptotic corpses were found entirely

89   within the HF stem and progenitor populations responsible for driving the next hair cycle.

90   To directly test the ability of HFSCs to clear apoptotic corpses, we devised a strategy to detect bona-

91   fide phagocytic cells within catagen-phase HFs. By activating Cre-recombinase in mid-growth HFs of

92   *Sox9CreER[+]*; *R26-Brainbow2.1[fl/+]* mice, we specifically labeled the upper ORS compartment with one of four

93   fluorophores (nuclear GFP, cytoplasmic YFP or RFP, and membrane CFP). Tracing these stochastically

94   labelled stem and progenitor cells across the hair cycle, we visualized apoptotic corpse engulfment of one

95   colour by phagocytic cells of another colour by both immunofluorescence imaging and fluorescent-activated

96   cell sorting (**Fig. 1c**). Wherever cell death was negligible, i.e. at the end of anagen and again during telogen,

97   double-positive cells were largely absent; however, double-positive cells rose markedly during the

98   destructive phase, peaking in late catagen.

99   Clearance of apoptotic corpses within the mature tissue appeared to necessitate a close spatial

100   relation between the nonmotile phagocyte and the dying cell, as evidenced by nearest apoptotic neighbour

101   analyses of phagocytic cells (**Fig. 1b,d, Extended data Fig. 1c**). Indeed, a majority of phagocytic ORS cells

102   were found either directly adjacent to or one cell body away from an apoptotic cell. Consistent with rapid

103   apoptotic cell recognition and clearance, few stand-alone apoptotic cells were identified per follicle, with

104   many more engulfed apoptotic bodies detected inside healthy basal ORS epithelial progenitors (**Fig. 1b,e**).

105   Indeed, TEM images of HFs in late catagen (CatVII) revealed an average of 2-3 apoptotic corpses per stem

106   or progenitor cell (**Fig. 1d, Extended data Fig. 1d**), suggestive of multiple rounds of engulfment. These

107   findings exposed HFSCs as a cohort of non-professional phagocytes, with important roles in both tissue

108   destruction and regeneration.

109

110   **Hair follicle stem cells adopt a transient phagocytic program characterized by *Mertk* expression**

111   The finding that HFSCs are important contributors to apoptotic cell clearance during catagen

112   prompted us to wonder how their phagocytic activity is controlled to prevent elimination of the stem cell pool.

113   To answer this question, we first turned to single-cell transcriptomic profiling of HFSCs across the hair cycle

114   to see if the program might be regulated transcriptionally. Applying the Leiden algorithm, we identified 7 cell

115   clusters which corresponded to hair cycle stage and anatomic location (**Fig. 2a**, **Extended Data Fig. 2**). To

116   determine the transcriptional shifts that accompany the transition from HF growth to regression, we

117   performed gene set enrichment analysis on differentially expressed genes from the end of the growth phase

118   (AnaVI) to mid-late destructive phase (CatVI-VII). Notably, the catagen-phase stem and progenitor cells

119   displayed a hair cycle-dependent significant enrichment of gene ontology terms related to a phagocytic state,

120   including apoptotic cell clearance, actin cytoskeletal rearrangement, phagocytic cup formation and trafficking

121   to the lysosome (**Fig. 2b, Extended Data Fig. 3a**).

122   Recognition of corpses by phagocytic cells involves the activation of apoptotic cell clearance

123   receptors, often by binding surface exposed phosphatidylserine (PS) on the apoptotic cell either directly or

124   via the engagement of bridging molecules[4-6] (**Fig. 2c**). To visualize the pattern of gene expression associated

125   with apoptotic cell clearance receptors and bridging ligands, we created aggregate gene set scores for these

126   terms and visualized them on the UMAP projected data. Strikingly, catagen HF stem and progenitor cells

127   were strongly enriched for both apoptotic cell clearance receptors and bridging molecule expression, with a

128   more modest increase in the lysosomal gene set (**Fig. 2d**, **Extended Data Fig. 3b**). Among the genes

129   differentially expressed in catagen were several members of the Tyro3/Axl/Mertk (TAM)-family receptor and

130   integrin receptor pathways of apoptotic cell recognition and tethering, including the receptors *Tyro3*, *Mertk,*

131   and *Itgav*, as well as the PS-bridging proteins *Gas6, Pros1, Mfge8* and *Thbs1* (**Fig 2d**, **Extended Data Fig.**

132   **3c**, **Supplemental Table I**)*.*

133   Turning to the physiological significance of our transcriptomic observations, we used FACS and

134   observed a significant enrichment of TAM-family surface expression on HF stem and progenitor cells that

135   had engulfed another cell (**Fig. 2e**, **Extended Data Fig. 4a**). FACS quantifications documented that surface

136   expression of TAM-family members peaked during catagen, but was largely absent at other phases of the

137   hair cycle (**Extended Data Fig. 4b,c**). A subset of these TAM-family[+] HFSCs also displayed an expanded

138   lysosomal compartment, indicative of apoptotic corpse degradation within phagolysosomes (**Extended Data**

139   **Fig. 4d**).

140   Interrogating the functional importance of our findings, we ablated *Mertk* in mice, and also blocked

141   exposed phosphatidylserine with intradermally-injected AnnexinV. Both of these measures resulted in

142   delayed apoptotic corpse clearance, with more unengulfed apoptotic cells and fewer phagocytic HF stem or

143   progenitor cells compared to controls (**Fig. 2f,g**). Taken together, these results provide compelling evidence

144   that HFSCs invoke a classical apoptotic cell clearance pathway, but do so transcriptionally and in a unique,

145   highly controlled transient manner to act as periodic phagocytes.

146

147   **RXRa is a master regulator of the phagocytic state in hair follicle stem cells**

148   The transient nature of the phagocytic program in HFSCs distinguished it from professional

149   phagocytes whose primary role is to clear dead cells. To understand how the phagocytic program is

150   dynamically regulated in tissue stem cells, we profiled the chromatin landscape of FACS-purified HFSCs at

151   the end of the growth phase and during apoptotic regression. Using an assay for transposase-accessible

152   chromatin by high-throughput sequencing (ATAC-seq) coupled with differential peak analysis, we identified

153   two sets of dynamic chromatin peaks: those that closed upon entry to catagen, and those that became

154   accessible (**Extended Data Fig. 5**).

155   Of note, genes in proximity to catagen-opening peaks encoded proteins associated with apoptotic

156   cell receptors, soluble PS-bridging molecules, phagocytic cup formation and phagolysosome maturation

157   (**Fig. 3a**). To identify candidate transcription factors mediating this dynamic chromatin accessibility, we

158   performed motif enrichment analysis for peaks that either opened or closed during the regressive phase. We

159   discovered that motifs belonging to the retinoid X receptor (RXR)-family of transcription factors were

160   significantly enriched in peaks gained in catagen (**Fig. 3a**). Notably, the most enriched RXR-family motif

161   among catagen-specific peaks was a direct-repeat 2 (DR2) motif composed of hexameric RXR binding motifs

162   separated by 2 nucleotides. This repeat has been implicated in RXR heterodimerization with retinoic acid

163   receptors (RARs)[16-18] (**Extended Data Fig. 6a**).

164   To test the hypothesis that RXR-RAR family members regulate the phagocytic machinery, we first

165   surveyed the expression of the entire nuclear receptor superfamily across the hair cycle. Of these, *Rxra* and

166   *Rarg* stood out as having appreciable expression that peaked at the height of apoptotic regression in the HF

167   (**Extended Data Fig. 6b**). Immunofluorescence confirmed the nuclear localization of both RARγ and RXRα

168   in the proximity of dying cells in catagen (**Extended Data Fig. 6c**,**d**).

169   If RXRα-RARγ is the signaling complex responsible for the dynamic regulation of the catagen-

170   triggered phagocytic program, changing the levels of RXRα (the obligate heterodimeric partner) should

171   impact this step. To do so, we first ectopically expressed RXRα in skin progenitors. Using our powerful

172   ultrasound-guided *in utero* lentiviral delivery method, we transduced skin progenitors of *K14rtTA* embryos

173   with a constitutively expressed RFP transduction control gene and a doxycycline-inducible human *RXRA*

174   transgene. We then administered doxycycline at the end of the morphogenesis growth phase of the first hair

175   cycle and followed the fate of *RXRA* super-activated HF stem and progenitor cells during catagen. Congruent

176   with a role for RXRα signaling in induction and/or maintenance of this transient phagocytic phase, catagen

177   ORS cells with higher RXRα more frequently contained engulfed apoptotic bodies than neighbouring

178   untransduced cells (**Fig. 3b**, **Extended Data Fig. 7a**). Relative to controls, HFSCs with elevated RXRα also

179   displayed significantly higher levels of TAM-family receptors, consistent with enhanced phagocytic ability

180   (**Fig. 3c**).

181   We next turned to evaluating the functional consequences of eliminating RXRα from catagen-phase

182   HFSCs. For this, we bred our tamoxifen-inducible *Sox9CreER;R26-YFP-floxed* reporter mice to *Rxra-floxed*

183   animals, administered tamoxifen at the end of anagen, and then assessed HFSC phagocytic ability during

184   the subsequent destructive phase. In the absence of RXRα, catagen HFs initiated apoptosis normally, but

185   were strikingly defective at clearing corpses (**Fig. 3d, Extended Data Fig. 7b,c**). Notably, significantly fewer

186   HF stem and progenitor cells contained engulfed corpses and correspondingly, interstitial spaces were

187   littered with apoptotic debris. This in turn attracted F4/80-positive macrophages, which contacted *Rxra*

188   conditional knockout HFs (**Fig. 3d**).

189   The appearance of macrophages suggested that the catagen HFSCs stopped functioning as non-
190 professional phagocytes in the absence of RXRα. Indeed, RXRα-deficient HFSCs failed to upregulate TAM-
191 family receptor expression in late catagen (**Fig. 3e**). To assess the ability of RXRα to regulate phagocytic
192 receptor expression directly, we mosaically transduced skin progenitors of *Sox9CreER; R26-LSL-Cas9-*
193 *EGFP* embryos with a lentivirus harboring an *Rxra*-targeting sgRNA and a mScarlet reporter, and then
194 administered tamoxifen at the end of the first anagen. By catagen, Scarlet⁺GFP⁺ cells, which had received
195 both sgRNA and activated Cas9, were largely deficient for RXRα protein and lacked TAM-receptors,
196 whereas single positive cells containing either active Cas9 or sgRNA maintained high levels of both RXRα
197 and surface TAM-family receptors (**Extended Data Fig. 7c**). Together, these data provided compelling
198 evidence that RXRα is required and sufficient to cell autonomously activate a phagocytic program in catagen-
199 phase HFSCs to clear apoptotic neighbours.

200   Given RXRα's role as a nuclear receptor, we next addressed whether RXRα participated in
201 transcriptional regulation of apoptotic cell clearance. To do so, we first assessed whether RXRα is
202 functionally important for opening the dynamic enhancer peaks that emerge during the transition from
203 anagen to catagen phases of the hair cycle. ATAC-seq and differential peak analyses of FACS-isolated late
204 catagen-phase HFSCs revealed that 8,311 peaks altered chromatin accessibility when *Rxra* was ablated,
205 while 4,222 peaks of these required RXRα for accessibility (**Extended Data Fig. 7d-h**). Notably, the
206 apoptotic cell clearance enhancer peaks were among the RXRα-dependent peaks which gained accessibility
207 during catagen (**Fig. 3f**).

208   Our data thus far suggested that RXRα specifically regulates the phagocytic transcriptome of HF
209 stem and progenitor cells, which should therefore be perturbed upon transcriptional antagonism of RXR-
210 family members. To test this hypothesis, we transiently administered the RXR antagonist HX531[18,19] during
211 catagen. In contrast to the vehicle control (injected into contralateral back skin), RXR-inhibition decreased
212 the number of phagocytic HFSCs and increased the number of unengulfed apoptotic corpses in late catagen
213 (**Extended Data Fig. 7i,j**). Similar to *Rxra* cKO animals, transcriptional antagonism of RXR led to decreased
214 TAM-family and *Mfge8* expression *in vivo*.

215   Together with expression patterns, these functional data strongly implicated RXRα-RARγ in the direct
216 regulation of a suite of apoptotic cell clearance genes necessary to transiently adopt a phagocytic state in
217 HF stem and progenitor cells. In this regard, it was intriguing that activities of RXRα with different nuclear
218 receptors have been reported to enhance the phagocytic program in macrophages[20-23]. Our findings highlight
219 an unexpected convergence between professional and non-professional phagocytes in how apoptotic cell
220 clearance is achieved at the transcriptional level, and suggest that by binding to different partners, RXRs
221 may fine-tune the regulation of this process to suit the needs of different tissues.

222

223 **RXRα-RARγ complex senses nearby corpses**

224   Efficient apoptotic cell clearance by non-professional phagocytes is still poorly understood. Early
225 embryonic epithelia appear to shuttle apoptotic corpses long distances to reach phagocytic trophoblast

226 cells[24]. By contrast, live imaging has indicated that embryonic and adult skin epithelia clear apoptotic corpses

227 that are in close proximity[13, 25]. Such observations suggest that spatially constrained epithelial cells harbor

228 the ability to efficiently sense, respond and clear neighboring apoptotic cells to deal with stochastic cell death.

229 To begin to identify the underlying mechanisms involved, we first examined the spatial relation

230 between apoptotic corpses and RXRα-RARγ during HF regression. Throughout catagen, many RXRα- and

231 RARγ-positive cells were found within one cell body distance of an unengulfed corpse (**Fig. 4a**, **Extended**

232 **Data Fig. 8a**). Probing this relation more deeply, we next ectopically induced apoptosis in telogen HFs by

233 sparsely activating diphtheria toxin subunit A (DTA) in a subset of HFSCs during the resting phase of the

234 hair cycle. This resulted in a dramatic rise in RXRα[+], TAM-family receptor[+] expression within the healthy

235 (DTA[neg]) HF stem and progenitor population (**Fig. 4b, Extended Data Fig. 8b**). Intriguingly, forced

236 overexpression of RXRα in the absence of apoptotic cells was not sufficient on its own to alter phagocytic

237 receptor expression from baseline (**Extended Data Fig. 8c**). Taken together, these results indicated

238 apoptotic corpses are an essential trigger for the activation of RXRα and the upregulation of TAM-family

239 receptors *in vivo*.

240 Given the close spatial relation between activation of RXRα-RARγ in HFSCs and apoptotic corpses

241 *in vivo*, we posited that HFSCs may be able to directly sense corpses without input from other cell types. To

242 test this, we cultured naïve telogen HFSCs and exposed them to apoptotic corpses. Within 30 minutes of

243 corpse addition, nuclear RXRα and RARγ were strongly elevated, followed by apoptotic cell engulfment

244 plateauing around 4-6 hours later (**Fig. 4c, Extended Data Fig. 8d**). Pre-treatment of apoptotic corpses with

245 either recombinant annexinV (to mask exposed phosphatidylserine) or BMS-777607 (to inhibit TAM-family

246 receptor activity) impaired their HFSC-stimulated engulfment, suggesting that a similar phagocytic program

247 was operative *in vitro* as *in vivo* (**Extended Data Fig. 8e**). Indeed, in response to corpses, cultured HFSCs

248 upregulated TAM-family receptor surface expression and engulfed apoptotic bodies both of which were

249 blocked by transcriptional antagonists against either RAR or RXR families, further consistent with the notion

250 that the phagocytic program is dependent upon apoptotic corpses and driven by RARγ-RXRα activities

251 (**Extended Data Fig. 8f**).

252 To directly assess the requirement for RXRα in mediating the response to corpses *in vitro*, we

253 cultured FACS-isolated YFP+ telogen-phase HFSCs from *Rxra* WT and cKO mice and transcriptionally

254 profiled them 4 hours after corpse addition. WT HFSCs responded to corpse exposure by transcriptionally

255 upregulating a cohort of phagocytic genes (**Supp Table for full list**). Notably, a subset of these genes

256 showed a markedly diminished response in *Rxra* null HFSCs concomitant with functionally impaired

257 apoptotic corpse clearance (**Fig. 4d,e**). Finally, although significantly affecting apoptotic corpse clearance

258 on its own, the RAR-family inhibitor AGN 193109 had no further effect on *Rxra* null cells, suggesting that the

259 two act cooperatively rather than in parallel (**Fig. 4e**, **Extended Data Fig. 8g**). Altogether, our culture data

260 demonstrated that HFSCs directly sense the presence of corpses and respond by upregulating a phagocytic

261 state that requires RXRα-RARγ signaling.

262

7

Hair follicle stem cells detect corpses via secreted signals to activate RXR-RAR activity

Macrophage elevation of TAM-family receptors via RXR-PPAR/LXR signaling requires engulfment and digestion of corpses[20-23]. By contrast, in HFSCs neither engulfment nor digestion of corpses was required for nuclear RXRα/RARγ or downstream TAM- family and lysosomal expression (**Extended Data Fig. 9a**). These data suggest that the mechanism of corpse activation of RXR signaling may differ in non-professional versus professional phagocytes and depends on both distinct co-receptors and ligands.

Interestingly, when we titrated apoptotic corpses to <1 per 100 HFSCs *in vitro*, we saw local increases in RXRα/RARγ-positive cells around each corpse (**Extended Data Fig. 9b**), reminiscent of that seen throughout catagen *in vivo*. That said, corpse-conditioned media increased the percentage of RXRα-positive cells to the same levels as corpses themselves, indicating that a secreted corpse factor(s) is signaling their presence (**Fig. 5a,b**). The best characterized "find-me" signals secreted by apoptotic cells are free nucleotides, sphingosine-1-phosphate (S1P) and lysophosphatidylcholine (LPC)[25-30]. Using small molecule inhibitors to block the generation of S1P (by inhibiting Sphk1/2 with MPA08), LPC (by inhibiting iPLA2 mediated phosphatidylcholine cleavage with bromoenol lactone, BEL) or free nucleotides (by inducing their degeneration with recombinant apyrase, Apyr), we found that of these three, LPC was the only one required to activate RXRα-RARγ (**Fig. 5a,b**). Correspondingly, blocking phosphatidylcholine cleavage by apoptotic corpses abolished both TAM and lysosome upregulation in HFSCs as well as corpse engulfment (**Fig. 5b**).

RNA sequencing verified that the effects of impairing phosphatidylcholine cleavage were at the transcriptional level, with moderate downregulation in a subset of apoptotic cell clearance receptors, PS-bridging proteins, actin cytoskeletal regulators involved in phagocytic cup formation, and mediators of phagolysosome maturation (**Extended Data Fig. 9c**). Finally, eliminating phosphatidylcholine cleavage/LPC production during catagen *in vivo* significantly diminished both RXRα upregulation in HF stem and progenitor cells adjacent to corpses, and also the number of corpse-containing HFSCs (**Fig. 5c**). By contrast, blocking the generation of S1P, free nucleotides, or exposure of phosphatidylserine *in vivo* showed no overt effect on RXRα activation or the phagocytic program (**Extended Data Fig. 9d**). Together, our data point to the view that in apoptotic cells, the cleavage of phosphatidylcholine to generate LPC and free fatty acids (FAs)[26,31] acts locally to activate RXR signaling and induce a phagocytic state in neighbouring HFSCs. Given that blood LPC levels are much higher than those derived from dying cells *in vivo*, a role for apoptotic cell-derived LPC in stimulating tissue phagocytes resolves the conundrum regarding its biological activity as a chemotactic molecule for circulating professional phagocytes [4,26,32-34].

Caspase-mediated activation of iPLA2 leads to hydrolysis of phosphatidylcholines at the sn-2 position, and subsequent release of LPC and free FAs[26,31,35]. A major constituent at the sn2 position in mammalian cell membrane phospholipids is the fatty acid arachidonic acid (AA)[36,37], which has been described as a natural ligand for RXR[38,39]. In this regard, adding recombinant AA and/or LPC elevated nuclear RXRα intensity in roughly 50% of cultured HFSCs across a physiologically relevant range of concentrations[26,40] (**Fig. 5d, Extended Data Fig 9e,f**).

299   In contrast to RXRα, RARγ did not respond to any concentration or combination of AA or LPC tested,

300   consistent with its classic ligands being 9-*cis* retinoic acid (9cRA)[41,42] and all-*trans* retinoic acid (ATRA)[43,44].

301   Notably, however, the combination of retinoic acid (RA) isomer and LPC (and/or AA) induced high levels of

302   both nuclear RXRα and RARγ in nearly all HFSCs *in vitro* (**Extended Data Fig. 9f**). Additionally, TAM

303   receptor expression comparable to corpse-exposure could be achieved by the combination of AA, LPC and

304   both RA isoforms (**Fig.5e**, **Extended Data Fig. 9g**). Optimal activation of the transcriptional phagocytic

305   program was also seen as judged by elevated transcripts for the TAM genes *Tyro3, Axl,* and *Mertk* and the

306   PS-bridging genes *Gas6, Mfge8 and Thbs1* (**Extended Data Fig. 9h**).

307   To unequivocally document and characterize the dependency of phagocytic program genes on

308   RXRα-RARγ activation, we used ATAC-seq and profiled WT and *Rxra* cKO HFSCs in two complementary

309   settings: 1) in response to corpses with (+VEH) or without (+BEL) phosphatidylcholine hydrolysis/LPC+AA

310   generation, and 2) in response to AA, LPC and RA combined. In the absence of corpses or signaling cocktail,

311   phagocytic genes were in a closed chromatin state (**Fig. 5f, Extended Data Fig. 10a-e**). Upon corpse

312   exposure, 12,614 peaks lost while 5,004 peaks gained accessibility. Approximately half of the peaks gaining

313   accessibility were markedly diminished upon *Rxra* ablation. These peaks were also sensitive to the presence

314   of LPC/FAs as documented by their decline upon exposure to BEL-treated corpses. Many of these peaks

315   resided within putative enhancers for genes involved in multiple stages of apoptotic cell clearance *in vivo* as

316   well as *in vitro* (compare **Figs. 3f** and **5f**). Impressively, the cocktail of AA, LPC and RA recapitulated the

317   effect of corpses on approximately one third of the RXRα-dependent peaks including those in enhancers of

318   genes encoding apoptotic cell recognition, engulfment, and processing pathways (**Fig. 5f, Extended Data**

319   **Fig. 10f**).

320   In summary, our findings reveal that tissue stem and progenitor cells can be stimulated by local

321   apoptotic corpse-derived factors to activate a phagocytic program that efficiently and expeditiously rids the

322   tissue of dying cells that might otherwise trigger an inflammatory response (**Fig. 5g**). We discovered that in

323   contrast to professional phagocytes, tissue stem cells fine-tune this program and are only diverted from their

324   normal tasks when they receive the right stimulatory signals. For the HF, these signals appear only

325   transiently in the destructive phase of the hair cycle when TGFβ causes cells within the HF to either terminally

326   differentiate (the hair shaft) or apoptose (the ORS)[13,45]. The stem cells maintain tissue homeostasis on

327   multiple fronts through a mechanism that is rooted in their ability to sense apoptotic corpse signals, primarily

328   the lipids LPC and AA, in combination with local tissue signals, e.g. retinoic acid. In combination, these

329   factors induce nuclear RXRα-RARγ signaling to orchestrate a transient phagocytic state in the epithelial

330   stem cells, which enables them to efficiently engulf and clear apoptotic cells in a highly localized and

331   temporally controlled manner.

332   We surmise that this method of sensing apoptotic corpses may be broadly applicable to non-

333   professional phagocytes in other epithelial tissues that have to balance sporadic cell death with maintaining

334   an intact barrier. Indeed, many of these tissues utilize the same phagocytic receptors and PS-bridging

335   molecules that converge on the general Rac1-Elmo-Dock pathway that mediates phagocytic cup formation

336 and subsequent phagolysosome maturation[46-53]. That said, the beauty of having the pathway dependent

337 upon RXRs is that while corpse-dependent production of lyso-lipids and free fatty acids is the universal

338 activator of this transcription factor, RXRs can heterodimerize with a diverse family of binding partners each

339 of which have their own specific small molecule ligands, differentially produced under different tissue

340 conditions. By having a combinatorial trigger, phagocytosis can be tailored to suit the specific needs of each

341 tissue. Additionally, the ability of stem and progenitor cells to serve as major contributors to apoptotic cell

342 clearance provides a powerful mechanism for maintaining tissue homeostasis while enabling stem cells to

343 reside in immune-privileged niches devoid of professional phagocytes.[46,54] The transient phagocytic state

344 we describe here, which is tuned specifically to the presence of nearby apoptotic corpses, offers an attractive

345 mechanism to balance phagocytic duties against the primary stem cell function of replenishing differentiated

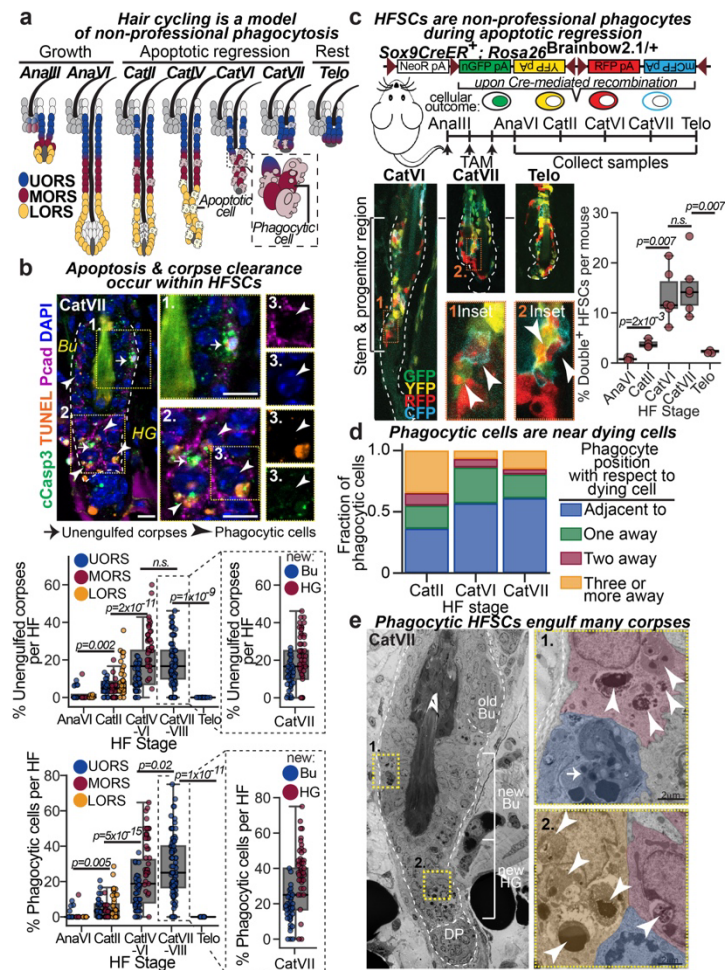346 cells to maintain tissue fitness.

347

Fig. 1 Apoptotic corpses are cleared by neighbouring hair follicle stem cells in late catagen. a, Schematic of mammalian hair cycle depicting the old HFSC niche (bulge) in grey and active niche in blue. Ana, anagen; Cat, catagen; Telo, telogen; UORS, upper ORS (cells 1-15 containing HFSCs); MORS, middle ORS (cells 16-30); LORS, lower ORS (cells 31+). **b,** Top, Sagittal skin sections showing apoptic cells (cCasp3+TUNEL+) encased by upper ORS catagen cells (cell membrane delineated by P-cadherin). DAPI, DNA. Insets show dying cells (arrows), adjacent to phagocytic cells (arrowheads). Quantifications shown below. 10-20 follicles per mouse, n=4-6 mice per stage. Bu, bulge (HFSCs); HG, hair germ (early progenitor cells). Dashed lines denote dermo-epithelial border. Scale bar 10um. **c,** Top, strategy to identify functional phagocytic HF stem and progenitor cells. Bottom left, immunofluorescence images of single+ (containing no corpses) and double+ (phagocytic) HF stem and progenitor cells in the upper ORS. Insets show higher magnification of double+ cells that arise from engulfing apoptotic corpses of a different colour (white arrowheads). Bottom right, FACS quantifications. n=4-6 mice per stage. **d,** Quantifications across the hair cycle of phagocytic cell position with respect to nearest apoptotic cell. 10-20 follicles per mouse, n=4-6 mice per stage. **e,** Ultrastructural images showing multiple apoptotic corpses (white arrowheads) inside late catagen HF stem and progenitor populations. Boxed regions are magnified at right. Pseudocoloured individual cells highlight the presence of phagocytic stem (1.) and progenitor (2.) cells containing engulfed corpses (white arrowheads) near apoptosing cells (white arrow). DP, dermal papilla. All quantifications, multiple pairwise Student's T-Tests, p-values indicated. n.s. not significant (p>0.05).

Fig. 2 Transient upregulation of phagocytic machinery mediates apoptotic cell clearance in catagen.
a, Left, strategy to profile hair follicle (HF) epithelial cells across the hair cycle using single-cell RNA-sequencing. Abbreviations as in Fig. 1. Right, UMAP representation and Leiden clustering of single-cell transcriptomes from pooled FACS-isolated CD34^{low} integrin$^+$ lower ORS and CD34^{high} integrin$^+$ upper ORS cells from wild-type mice. Cells are colour-coded by hair cycle stage and region, and Leiden clusters are encased by black dashed lines. **b,** Gene set enrichment analysis for genes upregulated in catagen versus late anagen; GO, gene ontology. **c,** Schematic depicting apoptotic cell recognition and tethering by neighbouring phagocyte. **d,** UMAP representation of single-cell transcriptomes coloured by aggregate gene set score, with insets showing the relative expression levels (log2[TPM+1]) of example genes from each gene set. The catagen cluster is outlined. Left, Apoptotic cell receptor genes. Right, Apoptotic cell ligands. **e,** *Tyro3*/*Axl*/*Mertk* (TAM)-family phagocytic receptor expression in FACS-purified *Sox9CreER$^+$ Brainbow2.1* fluorophore HFSCs that are double$^+$ (containing an apoptotic corpse) versus single$^+$ (no corpses) per mouse across the hair cycle, *n*=4-6 mice per stage. **f,** Left, Sagittal sections of catagen HFs from wild type (WT) versus constitutive *Mertk* knockout (KO) mice; boxed regions are magnified at right; cC3, cleaved caspase 3; Pcad, p-cadherin; scale bar 20um. Right, Quantifications of unengulfed apoptotic corpses (Top) and corpse-containing phagocytic HFSCs (Bottom). 20 follicles (CatIV-VI) and 65 follicles (CatVII-VII) quantified, *n*=3 mice per stage. **g,** Top, strategy to block corpse-exposed phosphatidylserine (PS) via intradermal injection of soluble AnnexinV (AnxV) during catagen. Contralateral vehicle injections as internal control. Quantifications of unengulfed apoptotic corpses (Bottom left) and corpse-containing phagocytic HFSCs (Bottom right). 5 follicles quantified per mouse, *n*=4 mice. All quantifications, multiple pairwise Student's *T*-Tests, p-values indicated. n.s. not significant (p>0.05).
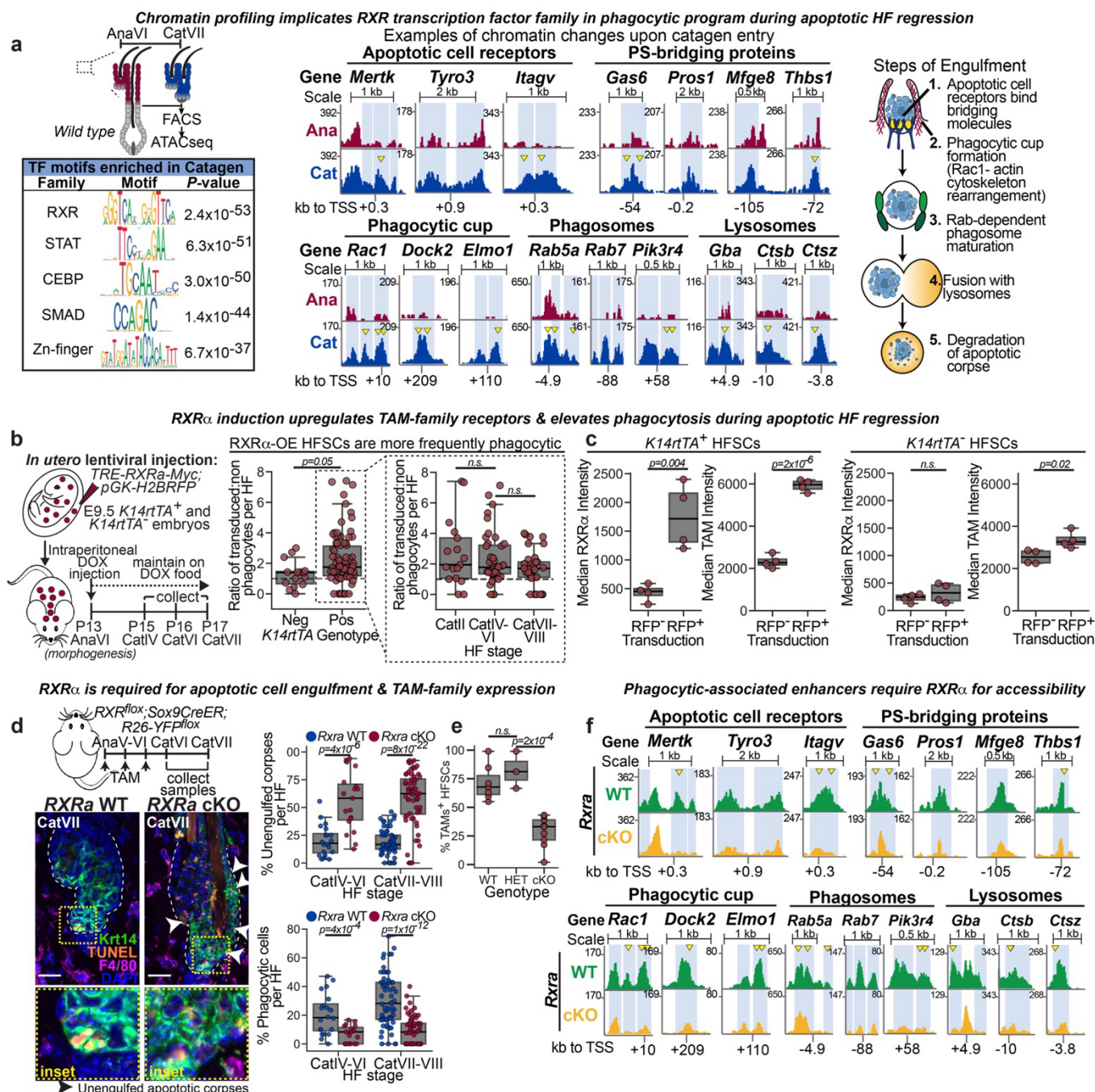
12

Fig. 3 RXRa is a master regulator of the phagocytic hair follicle stem and progenitor cell state. a, Top left, Strategy to profile FACS-isolated hair follicle stem cells (HFSCs) in late anagen (AnaVI) versus late catagen (CatVII) by ATAC-seq. Bottom left, Motif enrichment analysis on catagen accessible peaks. Middle, Replicate-pooled peak tracks for enhancers associated with phagocytic genes in catagen (Cat) versus anagen (Ana). Transcription start site, TSS. Phagocytic genes are grouped according to engulfment step (schematized at right). Differential peaks highlighted in light blue, yellow arrowheads point to RXR-family bound footprints. Peak tracks in reads per genome coverage (RPGC). **b,** Left, Inducible RXRα expression strategy. Middle, Quantification of untransduced versus transduced phagocytic cells. n=2-4 mice per stage, 8-10 HF analyzed per mouse. **c,** Quantifications of RXRα (left) and TAM-family (right) expression in FACS-isolated HFSCs. Data are paired, with untransduced (RFP⁻) and RXRa-overexpressing (RFP⁺) cells co-occuring, n=4 mice. Data for *K14rtTA*⁻ control right-most panels. **d,** Left top, *Rxra* conditional knockout (cKO) strategy. Left bottom, Sagittal sections of late catagen *Sox9CreER;Rxra^{fl/fl};R26-YFP^{fl/+}* skins. wild type, WT; Scale bar 20um. Right, Quantifications of unengulfed apoptotic bodies (top) and HFSCs containing corpses (bottom). 10-15 follicles analyzed per mouse, n=6-8 mice per genotype. **e,** Percentage of FACS-isolated TAM-family⁺ HFSCs per mouse for *Rxra* WT, heterozygous (HET) and cKO. n=3-8 mice per genotype. **f,**

13

414 ATAC-seq pooled replicate peak tracks covering the enhancers in (a) for FACS-isolated CatVII HFSCs,
415 scaled, normalized and annotated as in (a). All quantifications, multiple pairwise Student's *T*-Tests, p-values
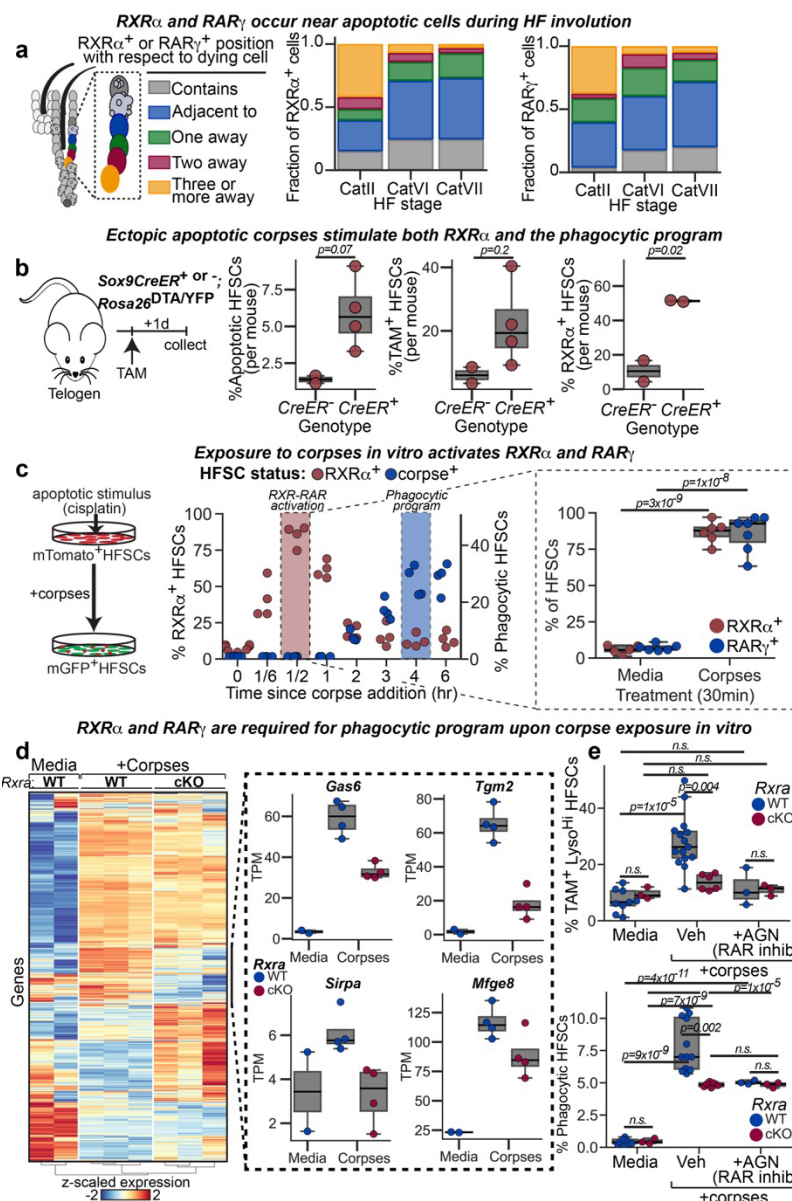416 indicated. n.s. not significant (p>0.05).
417

Fig. 4 RXRα responds to corpse-derived signals to upregulate the phagocytic program. a, Left, Schematic of cell position with respect to nearest corpse. Fractions of RXRα⁺ (Middle) or RARγ⁺ (Left) position in relation to corpses across catagen. n= 300 cells across 3 mice per stage. **b,** Left, Induction of corpses in quiescent hair follicles (HFs). Right, Quantifications of total FACS-isolated HFSCs that are apoptotic (AnnexinV⁺), TAM-family⁺, and RXRα⁺ per mouse in control (*Sox9CreER⁻*) or corpse-positive (*Sox9CreER⁺*) animals. n= 2-4 animals per genotype. **c,** Left, *In vitro* strategy to expose naïve HFSCs to corpses directly. Middle, Time-course quantification of total HFSCs that are RXRα⁺ (red) versus containing a corpse (blue). Right, Quantification of RXRα⁺ and RARγ⁺ HFSCs at 30 min. post corpse addition. n=4-6 experiments per time point, performed in triplicate. **d,** Bulk RNA-squencing of *Rxra* wild type (WT) versus conditional knockout (cKO) HFSCs in media or upon corpse exposure. Left, Heatmap of differentially expressed genes (full list in Supplemental Table 4); Z-scaled expression scores of genes (rows; blue, downregulated; red, upregulated) by experimental replicates (columns; n=2-3 WT, 3 cKO). Right, Expression of phagocytic genes; TPM, transcript per million. **e,** Quantification of total HFSCs in culture that are both TAM-family⁺; Lysosome^high (top) or contain engulfed corpses (bottom) 4 hours post corpse addition to RXRα WT or cKO with or without RAR-family inhibition (+AGN condition). Data from n=3-8 experiments per genotype per condition, averaged across triplicates. All quantifications, multiple pairwise Student's *T*-Tests, p-values indicated. n.s. not significant (p>0.05).
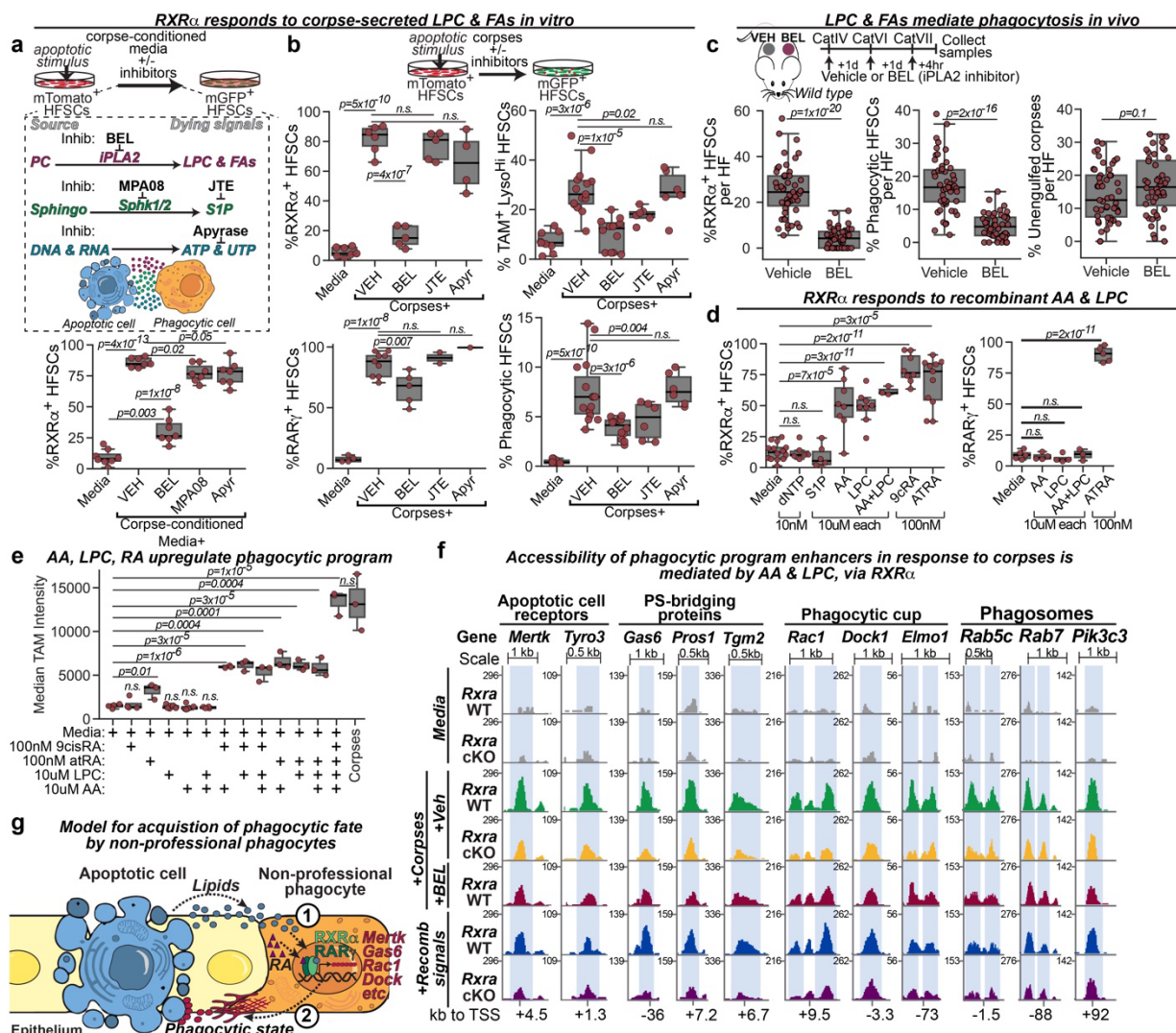
15

471

Fig. 5 Corpse-derived lysophosphatidylcholine and fatty acids are necessary and sufficient for RXRα-mediated regulation of the phagocytic program. a, Top, Schematic of secreted signals from dying HFSCs; Inhib, inhibitors; BEL, bromoenol lactone; PC, phosphatidylcholine; LPC, lysophosphatidylcholine; FAs, fatty acids; JTE, JTE013; Sphingo, sphingosine; S1P, sphingosine-1-phosphate. Bottom, Quantification of RXRα$^+$ HFSCs responding to corpse-conditioned media. Apyr, Apyrase; n=7 experiments per condition. **b,** Top, Experimental schematic. Left, Percentages of RXRα$^+$ (Middle) and RARγ$^+$ (Bottom) HFSCs per experiment, 30 min. post corpse addition. n= 4-6 experiments per condition, as averaged triplicates. Right, Percentages of TAM-family$^+$; Lysosome^{high} HFSCs (Middle) and corpse-containing HFSCs (Bottom) per experiment, 4 hours post corpse addition. n= 6-12 experiments per condition. **c,** Top, Strategy to inhibit production of LPC and FAs during catagen by intradermal injections of the iPLA2 inhibitor BEL in WT mice. Contralateral vehicle injections serve as control, n= 6 mice. Bottom, Percentages of RXRα$^+$ cells (Left), corpse-containing HFSCs (Middle), and unengulfed apoptotic bodies (Right) per HF. n=6-8 follicles quantified per condition per mouse, n=6 mice. **d,** Percentage of RXRα$^+$ (Left) and RARγ$^+$ (Right) HFSCs per experiment, 30 min after addition of the indicated recombinant molecules; dNTP, 10nM each dUTP and dATP; AA, arachidonic acid; 9cRA, 9-*cis* retinoic acid; ATRA, all-*trans* retinoic acid. n=4-12 experiments per condition, as averaged triplicates. **e,** FACS quantification of TAM-family expression on HFSCs treated with the indicated recombinant molecules compared to TAM expression post corpse exposure, all 4 hours later. n=3-6 experiments per condition. **f** ATAC-seq replicate-pooled peak tracks for enhancers associated with phagocytic genes in cultured *Rxra* WT and cKO HFSCs exposed to apoptotic corpses with (+Veh) or without (+BEL) secreted LPC and FAs, or treated with retinoic acid+LPC+AA (+Recomb signals) for 4 hours. Peaks with differential accessibility highlighted in light blue. Peak tracks in reads per genome coverage (RPGC). Lysosome-associated peaks in Extended Data Fig. 10. **h,** Model by which HFSCs sense apoptotic corpses

16

494   via secreted LPC and FAs, and activate RXR-RAR signaling to adopt a transient phagocytic fate. All
495   quantifications, multiple pairwise Student's *T*-Tests, p-values indicated. n.s. not significant (p>0.1).

496
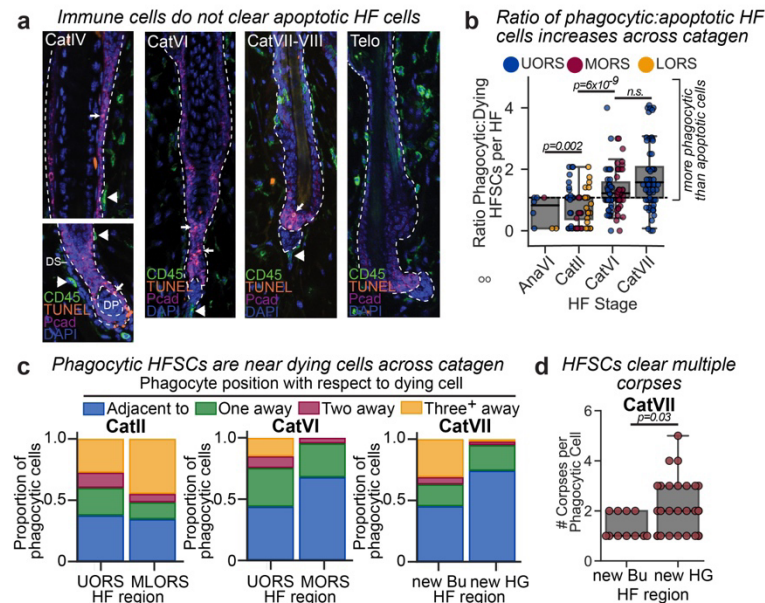
Extended Data Fig. 1 *(Related to Fig.1)* **Apoptotic corpses are cleared by neighbouring hair follicle stem cells in catagen. a,** Sagittal skin sections of CD45+ immune cells in the dermis (white arrowheads) that do not contact TUNEL+ apoptotic corpses (white arrows) within the regressing hair follicle, outlined by P-cadherin (Pcad, purple). Cat, catagen stage; Telo, telogen. Images are representative of 25-30 follicles across 3 mice per stage. Dashed lines denote dermo-epithelial border. **b,** Ratio of phagocytic to apoptotic cells per hair follicle (HF) across the hair cycle. 10-20 follicles were quantified per mouse, *n*=4-6 mice per stage. **c,** Quantification of HF phagocytic cell position with respect to nearest apoptotic cell, broken down by position within the outer root sheath (ORS). UORS, upper ORS; MLORS, middle and lower ORS; MORS, middle ORS; Bu, bulge; HG, hair germ. **d,** Quantification of the number of apoptotic corpses contained per phagocytic stem (new Bu, new bulge) and progenitor (new HG, new hair germ) cell via transmission electron micrography. *n*=7 hair follicles from 2 wild type mice. All quantifications, multiple pairwise Student's *T*-Tests, p-values indicated. n.s. not significant (p>0.05).

18

509
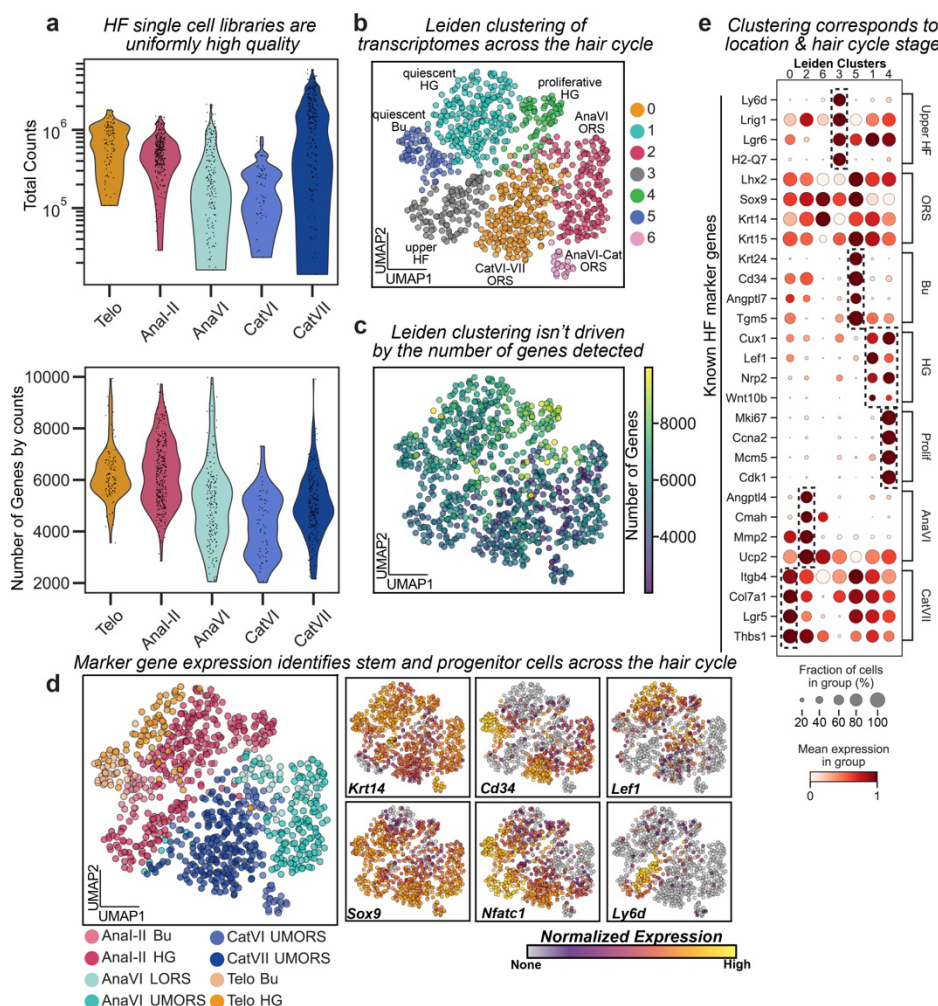
Extended Data Fig. 2 *(Related to Fig. 2)* **Single-cell RNA-sequencing of hair follicle epithelial cells across the hair cycle. a,** Total counts per cell (Top) and number of genes detected per cell (Bottom) for single-cell transcriptomic libraries across the hair cycle. Telo, telogen; AnaI-II, early anagen; AnaVI, late anagen; CatVI-VII, mid-late catagen. **b,** Uniform manifold projection (UMAP) representation of single cell transcriptomes coloured according to Leiden-based clustering algorithm. Cluster colour legend is at right, putative cluster identity based on hair follicle (HF) cycle stage and marker gene expression annotated on UMAP. **c,** UMAP representation of the number of genes detected per cell (colourbar legend at right). **d,** Left, UMAP representation coloured by anatomic location (via FACS antibody markers) and hair cycle stage. Bu, bulge; HG, hair germ; LORS, lower outer root sheath (ORS); UMORS, upper-middle ORS. Right, UMAPs of relative expression levels (log2[TPM+1]) of selected marker genes. ORS markers: *Krt14, Sox9*; Bu hair follicle stem cell (HFSC) markers: *Cd34, Nfatc1*; HG progenitor marker: *Lef1*; Upper HF marker: *Ly6d*. **e,** Dot plot representation of expanded marker gene analysis across Leiden clusters, with each vertical column corresponding to one grouped Leiden cluster and each horizontal row representing a marker gene. Marker genes are organized according to their reported function and location with the hair cycle; Prolif, proliferation. Dot size corresponds to the fraction of cells expressing each gene. Dot colour corresponds to normalized mean expression level within each cluster.

526

19
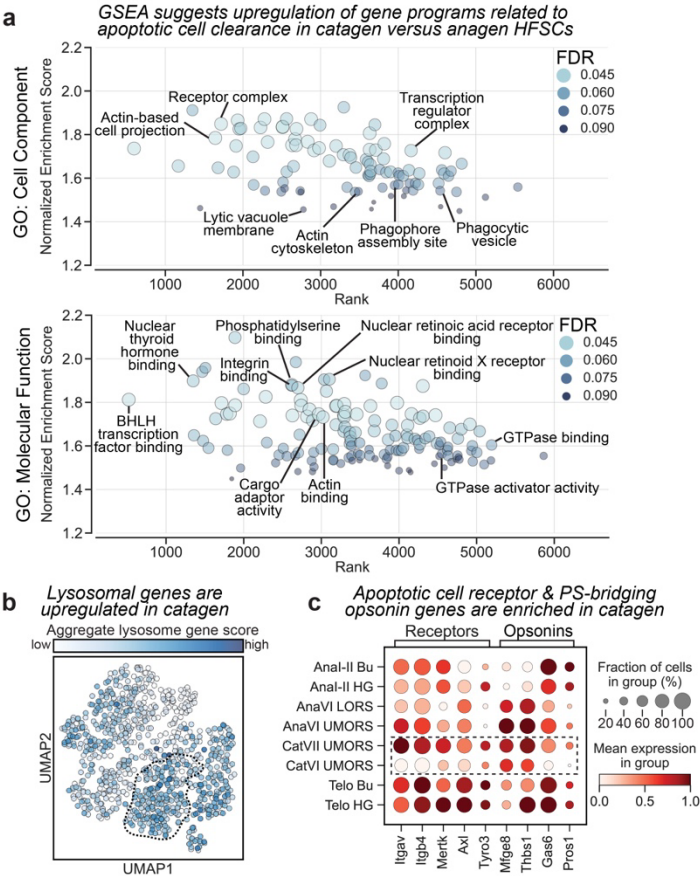
Extended Data Fig. 3 *(Related to Fig. 2)* **Gene set enrichment identifies pathways related to apoptotic cell clearance upregulated in catagen hair follicle stem and progenitor cells. a,** Visual representation of all gene sets identified as upregulated in catagen versus anagen (FDR <0.1), broken by Gene Ontology (GO) category. Gene set enrichment analysis (GSEA) ranks gene set terms by position at which maximum enrichment occurs (horizontal axis), and by normalized enrichment score (vertical axis). Dot colour and size reflects the False Discovery Rate (FDR) calculated for each gene set (legend inset). Selected gene sets related to apoptotic cell clearance are annotated. See Supplementary Tables 1 and 2 for full lists. **b,** UMAP representation of single-cell transcriptomes coloured by aggregate lysosomal gene set score shows enrichment in the catagen cluster (dashed black outline).**c,** Dot plot representation of selected apoptotic cell recognition receptors and phosphatidylserine-bridging genes (vertical columns) across hair cycle stages (horizontal rows). Each dot represents the fraction of cells (size) and normalized mean expression (colour) of a single gene across the hair cycle grouped single cell transcriptomes.
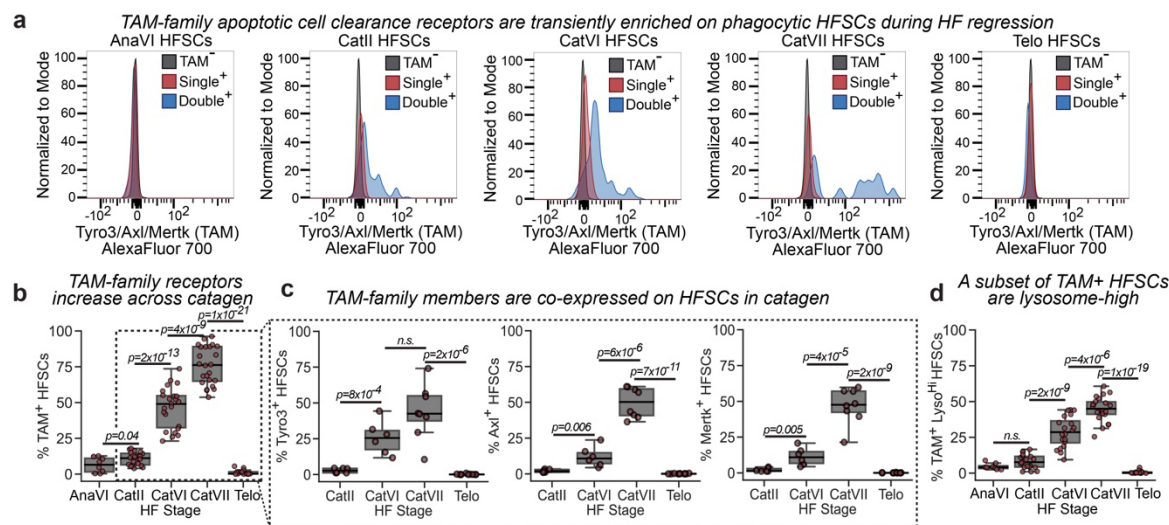
Extended Data Fig. 4 *(Related to Fig. 2)* **TAM-family receptor pathway for apoptotic cell engulfment is expressed in hair follicle stem and progenitor cells during apoptotic regression. a,** FACS plots showing normalized counts of cell-surface expression of *Tyro3/Axl/Mertk* (TAM)-family receptors on hair follicle stem cells (HFSCs) across the hair cycle, from the end of anagen growth phase (AnaVI), through early (CatII), mid (CatVI) and late catagen (CatVII) to quiescence (Telo, telogen). *Sox9CreER*[+] was used to drive *Brainbow2.1* fluorophore reporter expression so that all HFSCs are stochastically labeled with a single fluorophore (single+) and only phagocytic HFSCs (containing an apoptotic corpse of a different colour) can be double+. See supplemental methods for FACS sorting scheme. $n=$ 4-6 mice analyzed per stage. Data is quantified in Fig. 2d. **b,** Percentage of TAM-family[+] HFSCs per mouse across the hair cycle. $n=$8-16 mice per hair follicle (HF) stage. **c,** Percentage of FACS-isolated HFSCs expressing each individual TAM-family member (Tyro3, left; Axl, middle; Mertk, right) during catagen. $n=$ 6-10 mice analyzed per stage. **d,** Percentage of HFSCs which are TAM[+] and lysosome[high] across the hair cycle. $n=$ 8-16 mice per stage. All quantifications, multiple pairwise Student's *T*-Tests, p-values indicated. n.s. not significant ($p>0.05$).
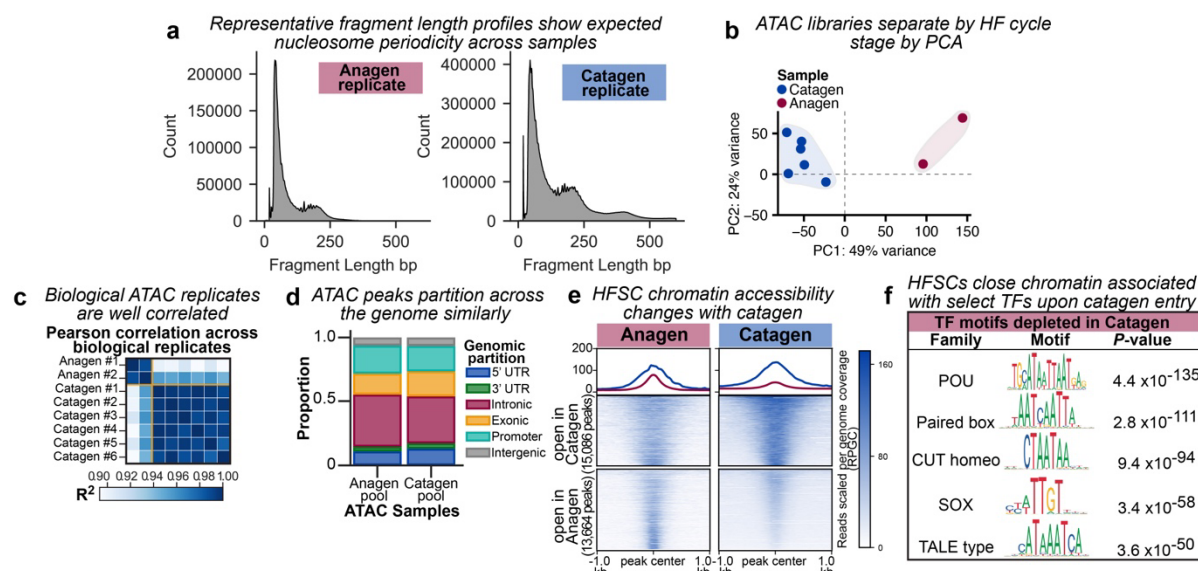
555
556
557 **Extended Data Fig. 5** *(Related to Fig. 3)* **Profiling hair follicle stem cells from growth to regression**
558 **reveals a shift in chromatin accessibility associated with apoptotic elimination. a,** Representative
559 histograms of fragment lengths in base pairs (bp) detected per biological replicate for each hair cycle stage
560 examined by ATAC-seq. Nucleosome-free, mono- and di-nucleosome peaks were identifiable for all
561 replicates analysed. **b,** Principal component analysis on reads mapped to peaks separates ATAC-seq
562 biological replicates by hair follicle (HF) cycle stage; n=2 (anagen) and n= 6 (catagen) **c,** Pearson correlation
563 (R^2) values for reads mapped to peaks across replicates. **d,** Bar graph of peaks partitioning across the
564 genome. **e,** Heatmap showing all peaks with significantly altered accessibility between anagen and catagen
565 replicates. Accessibility signal for pooled replicate samples is normalized for fraction of reads in peaks, and
566 scaled to reads per genome coverage (RPGC) (colourbar legend, right). Each row corresponds to a detected
567 peak, centered and extended +/- 1kb. Peaks are clustered based on differential accessibility, and
568 summarized as the mean accessibility signal per region in a blue line (peaks gaining accessibility in catagen)
569 or a pink line (peaks losing accessibility in catagen) in the graph at top. **f,** Motif enrichment analysis of the
570 13,664 peaks losing accessibility in catagen replicates suggests chromatin containing POU-domain
571 transcription factor motifs, among others, is specifically closed relative to the end of anagen. See
572 Supplemental Table 3 for full list.
573

22
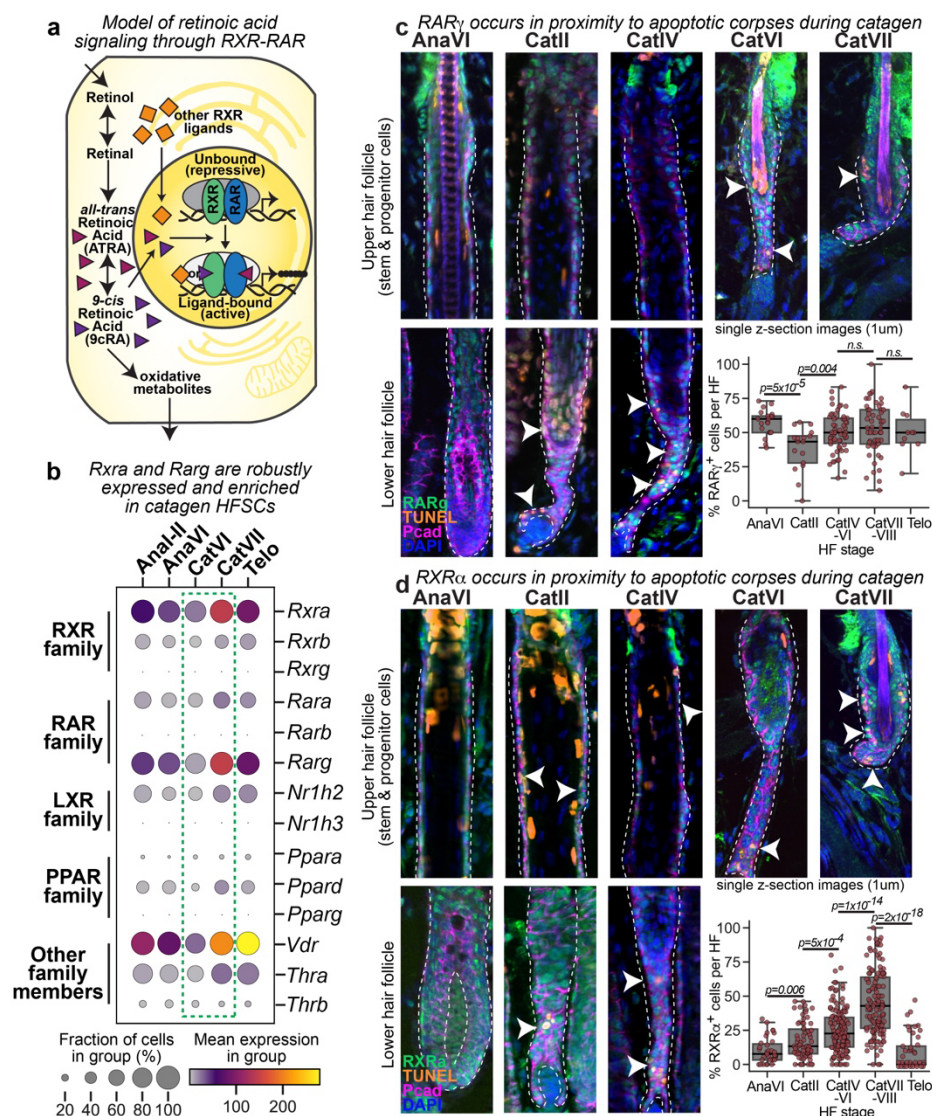
Extended Data Fig. 6 *(Related to Fig. 3)* **RXR and RAR family members are expressed in proximity to corpses during apoptotic regression. a,** Schematic depicting retinoid X receptor (RXR) and retinoic acid receptor (RAR) transcription factor signaling. **b,** Dot plot summarizing non-steroidal nuclear hormone receptor family expression across the hair cycle from single cell transcriptomic data. Each column shows aggregate expression for cells within a hair cycle stage, with dot size corresponding to the percentage of cells within the group expressing the gene and dot colour corresponding to mean normalized counts. **c, d,** Sagittal skin sections of RARγ$^+$ cells (**c**) and RXRα$^+$ cells (**d**) within hair follicles (dashed white outline) from the end of anagen growth phase (AnaVI) throughout catagen (Cat). Dashed line denotes epithelial-dermal border. Pcad, p-cadherin. Images are representative of 10-20 follicles analyzed per mouse, n=3-6 mice per hair cycle stage. Quantifications based on images above. All quantifications, multiple pairwise Student's *T*-Tests, p-values indicated. n.s. not significant (p>0.05).

23
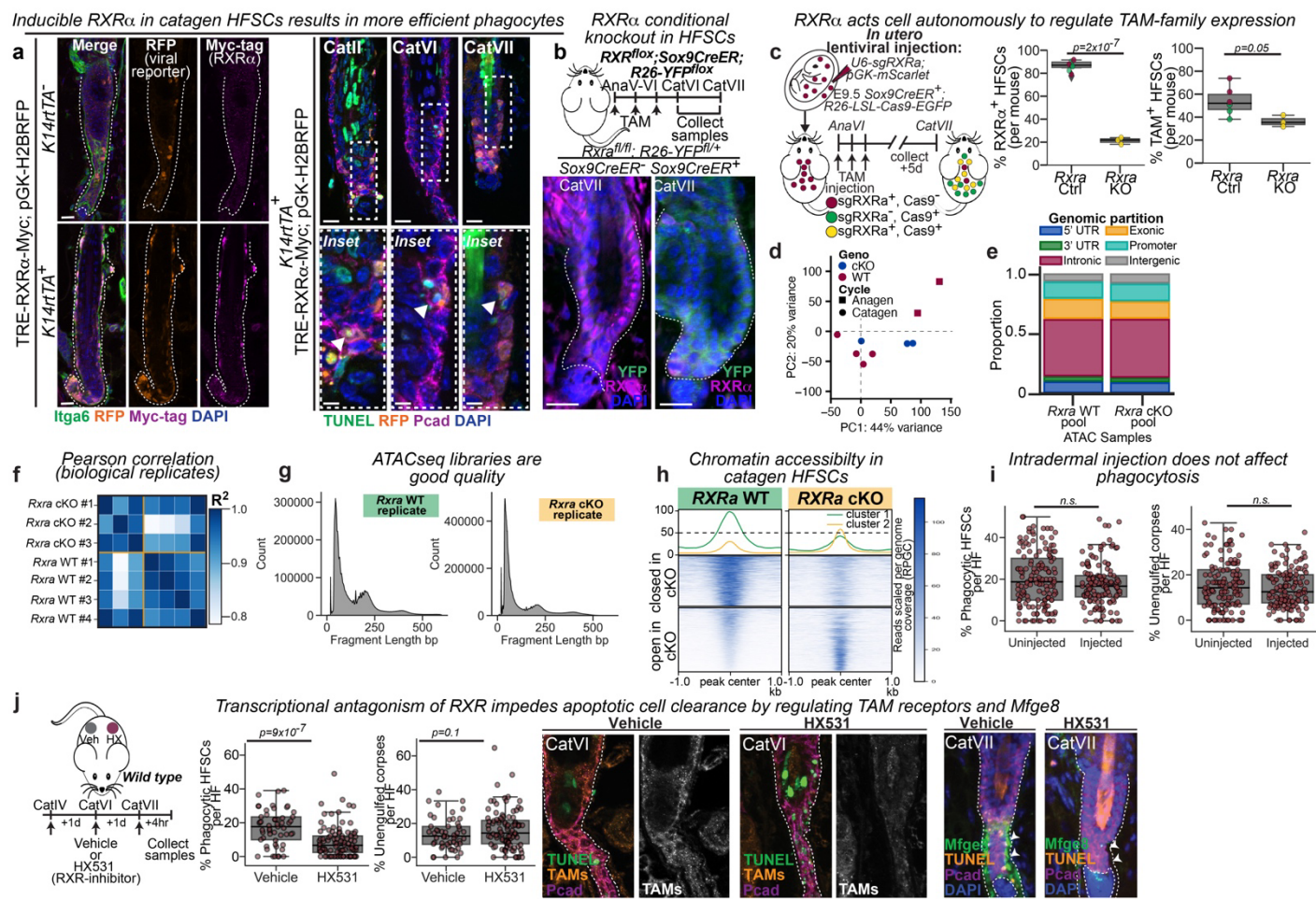
Extended Data Fig. 7 *(Related to Fig. 3)* **RXRα regulates the apoptotic cell clearance program *in vivo*.** **a,** Sagittal skin sections of *K14rtTA* mice injected with doxycycline (DOX)-inducible *TRE-Rxra-Myc*-tagged lentivirus containing constitutive H2B-RFP infection reporter (TRE-RXRa-Myc;pGK-H2BRFP). Left, DOX treatment induces Myc-tagged RXRα expression only in *K14rtTA*+ animals. Scale bar 20um. Right, *K14rtTA*+ RFP+ (RXRα-high) cells more often contain TUNEL+ corpses than non-transduced (RFP-) neighbouring cells. Scale bar 20um. Insets, magnified regions of the white dashed box region. Scale bar 10um. Images representative of 10-20 follicles per mouse, *n*=3 mice per genotype per catagen stage. **b,** Top, Experimental strategy. Bottom, Sagittal skin sections of *Rxra* wild type (WT, *Sox9CreER*-) and conditional knockout (cKO, *Sox9CreER*+) show loss of RXRα in YFP+ cKO. **c,** Left, Strategy to mosaically knockout (KO) RXRα by lentiviral injection of single guides against *Rxra* (sgRXRα) with mScarlet transduction reporter into *Sox9CreER*+; *R26-floxed-Cas9-EGFP* mice. Tamoxifen, TAM. Right, Percentages of RXRα+ HFSCs (Top) and TAM+ HFSCs (Bottom) per mouse. n=3 mice. **d,** Principal component analysis on reads mapped to peaks. **e,** Bar graph of peaks partitioning across the genome. **f,** Pearson correlation (R^2) values for *Rxra* WT and cKO ATAC-seq replicates. **g,** Representative histograms of fragment lengths in base pairs (bp) for *Rxra* WT and cKO HFSCs. **h,** Heatmap of differentially accessible peaks in late catagen HFSCs between *Rxra* WT and cKO pooled replicates, annotated as in Extended Data Fig. 5e. Reads per genome coverage, RPGC; colourbar legend, right. Differential peaks are summarized as mean accessibility signal per region in a yellow line (peaks opening in cKO) or a green line (peaks closing in cKO) in the graph at top. **i,** Percentages of phagocytic HFSCs (left) and unengulfed corpses (right) per late catagen HF (CatVII), either uninjected or intradermally injected with vehicle. n=125-150 HFs across 4-6 mice per condition. **j,** Left, Strategy to transiently inhibit RXR-family transcriptional activity by HX531 intradermal injection. Contralateral backskin was injected with vehicle (Veh) control. Middle, Percentages of corpse-containing HFSCs (Left) and unengulfed corpses (Right) per HF. n=10-15 HFs per mouse; n=8 mice. Right, Sagittal sections of contralateral vehicle- and HX531-injected back skin stained as indicated. Images are representative of n= 10-12 HFs per mouse, n=4 mice per staining panel. All quantifications, multiple pairwise Student's *T*-Tests, p-values indicated. n.s. not significant (p>0.1).
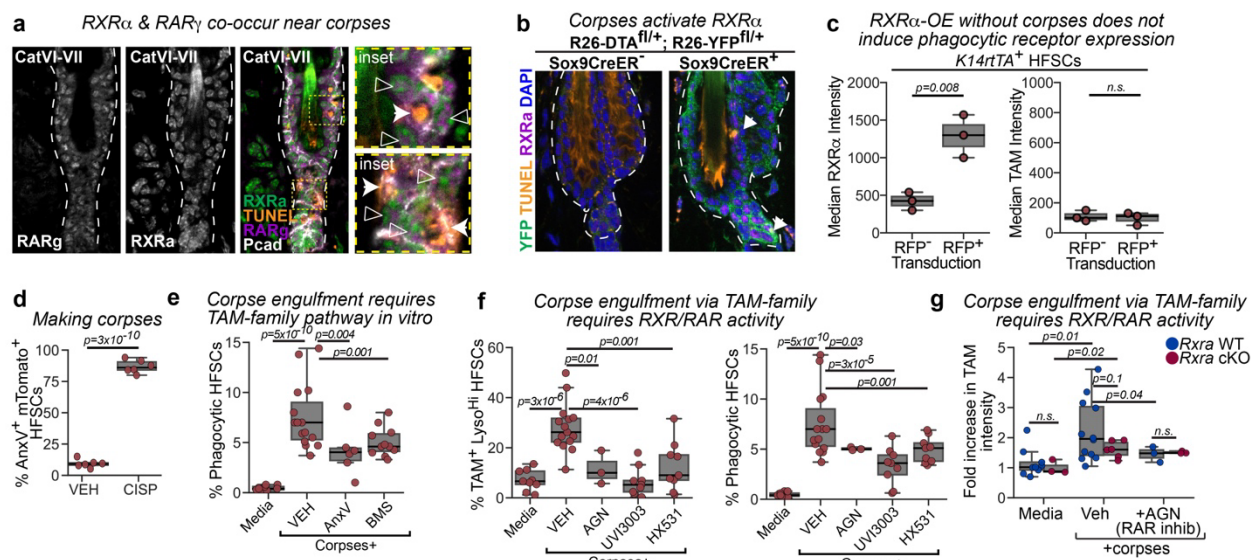
Extended Data Fig. 8 *(Related to Fig. 4)* **RXRα responds to corpses. a,** Representative immunofluorescence images for data in Fig. 4a. Nuclear RXRα and RARγ co-occur (open arrowheads) near unengulfed dying cells (closed arrowheads) in mid- late catagen hair follicles (HFs) (white dashed outline). Insets, higher magnification view of yellow boxed regions to left. 10-20 HFs per mouse, n=3-4 animals per hair cycle stage. **b,** Representative immunofluorescence images for FACS-quantified data in Fig. 4b. Diptheria toxin A (DTA) expression in *Sox9CreER*[+] mice creates TUNEL[+] corpses (white arrowhead) in quiescent HFs (white dashed outline), which induces nuclear RXRα. 10-20 HFs analyzed per mouse, n=3-4 animals per genotype. **c,** Quantifications of RXRα intensity (Left) and TAM-family expression (Right) for FACS-isolated hair follicle stem cells (HFSCs) from *K14rtTA*[+] mice induced to overexpress RXRα (RFP[+]) at the end of catagen and followed to early anagen (AnaII-III), using the same experimental strategy shown in Fig. 3b. n=3 mice. **d,** FACS-based percentage of mTomato[+] HFSCs undergoing apoptosis (AnnexinV[+]) in preparation of corpses/corpse-conditioned media. CISP, cisplatin. n=6 replicates. **e,** Percentage of corpse-containing HFSCs, 4 hours post corpse addition, requires phosphatidylserine exposure (blocked by addition of AnnexinV [AnxV]) and TAM-family activity (inhibited by addition of BMS-777607 [BMS]). n=6 replicates (AnxV) and n=12 replicates (BMS). **f,** FACS-based quantifications of the percentage of total HFSCs which are TAM-family[+], lysosome[high] (left) or contain corpses (right) 4 hours post corpse addition. Inhibition of RAR-family activity by AGN193109 (+AGN), or of RXR-family activity by UVI3003 or HX531. Note, both Media and Corpses+ VEH (vehicle) conditions are the same data as presented in (e), as experiments were carried out together. **g,** FACS-based quantification of TAM-family expression levels, normalized to median expression in media, for *Rxra* wild type (WT) or conditional knockout (cKO) HFSCs 4 hours after corpse addition. All quantifications, multiple pairwise Student's *T*-Tests, p-values indicated. n.s. not significant ($p>0.1$).

25

a *Engulfment isn't required for RXRα/RARγ activation*

b *Corpse proximity dependent activity of RXRα &RARγ*

c *A subset of the corpse-induced phagocytic program depends on iPLA2-mediated release of LPC & FAs*

d *RXRa activity does not require S1P, PS, or dNTPs in vivo*

Intradermal injection RXRα control

e *RXRa responds to recombinant AA & LPC*

f *RXRa &RARg responds to RA plus AA & LPC*

g *RA plus AA & LPC is sufficient to increase TAM-receptors*

h *RA plus AA & LPC is sufficient to increase phagocytic genes transcriptionally*

638 **Extended Data Fig. 9** *(Related to Fig. 5)* **Corpses secrete lysophosphatidylcholine and free fatty acids**
639 **to activate RXRα. a,** Quantifications of RXRα$^+$ (Top) and RARγ$^+$ (Middle) HFSCs 30 minutes following
640 addition of corpses with (+VEH) or without exposed phosphatidylserine (PS) (+AnxV), or in the presence of
641 TAM-family inhibitor BMS-777607 (+BMS). Bottom, Percentage of TAM-family$^+$;Lysosome^{high} HFSCs 4
642 hours after corpse exposure. *n*=4-8 replicates. **b,** Immunofluorescence of HFSCs stained for RXRα or RARγ
643 30 minutes after low-titre corpse addition. Insets are RXRα or RARγ alone. Scale bar, 10um. Representative
644 of triplicate experiments performed *n*=3 times. **c,** Left, Heatmap of bulk RNA-sequencing of wild type HFSC
645 replicates exposed to corpses with (+Veh, vehicle) or without (+BEL, bromoenol lactone) secreted
646 lysophosphatidylcholine (LPC) and fatty acids (FAs). Colour bar, Z-score normalized expression. Right,
647 Transcript per million (TPM) expression values of selected phagocytic program genes. Full list in
648 Supplemental Table 5. **d,** Strategy (Left) and percentages of RXRα$^+$ HFSCs (Middle) to manipulate corpse-
649 derived sphingosine-1-phosphate (S1P) (left), secreted nucleotides (middle), or exposed
650 phsophatidyleserine, PS, (right) by intradermal injections. Contralateral back skin was injected with vehicle
651 (Veh) control. Right, Uninjected versus vehicle-injected percentage of RXRα$^+$ cells. *n*=5-10 HFs per mouse,

26

652   3-6 mice per experiment. **e,** Percentage of RXRα$^+$ HFSCs in response to recombinant molecules. dATP &
653   dUTP, dNTP; arachidonic acid, AA; 9cRA, 9-*cis* retinoic acid; ATRA, all-*trans* retinoic acid. *n*=4-12 replicates
654   per condition. **f,** Percentage of HFSCs responding to recombinant molecules by increasing RXRα$^+$ cells (left)
655   or RARγ$^+$ cells (right). *n*=2 replicates per condition, averaged across technical triplicates. **g,** Percentage of
656   TAM-family$^+$ HFSCs in response to recombinant molecule combinations. *n*=3-6 replicates per condition. **h,**
657   Quantitative RT-PCR for phagocytic gene transcripts, relative to B2-microglobulin (*B2m*) levels, and
658   normalized to media-only conditions. Concentrations of indicated added molecules are as in (f,g). *n*=3
659   experimental replicates, performed in technical triplicates. All quantifications, multiple pairwise Student's *T*-
660   Tests, p-values indicated. n.s. not significant (p>0.1).
661
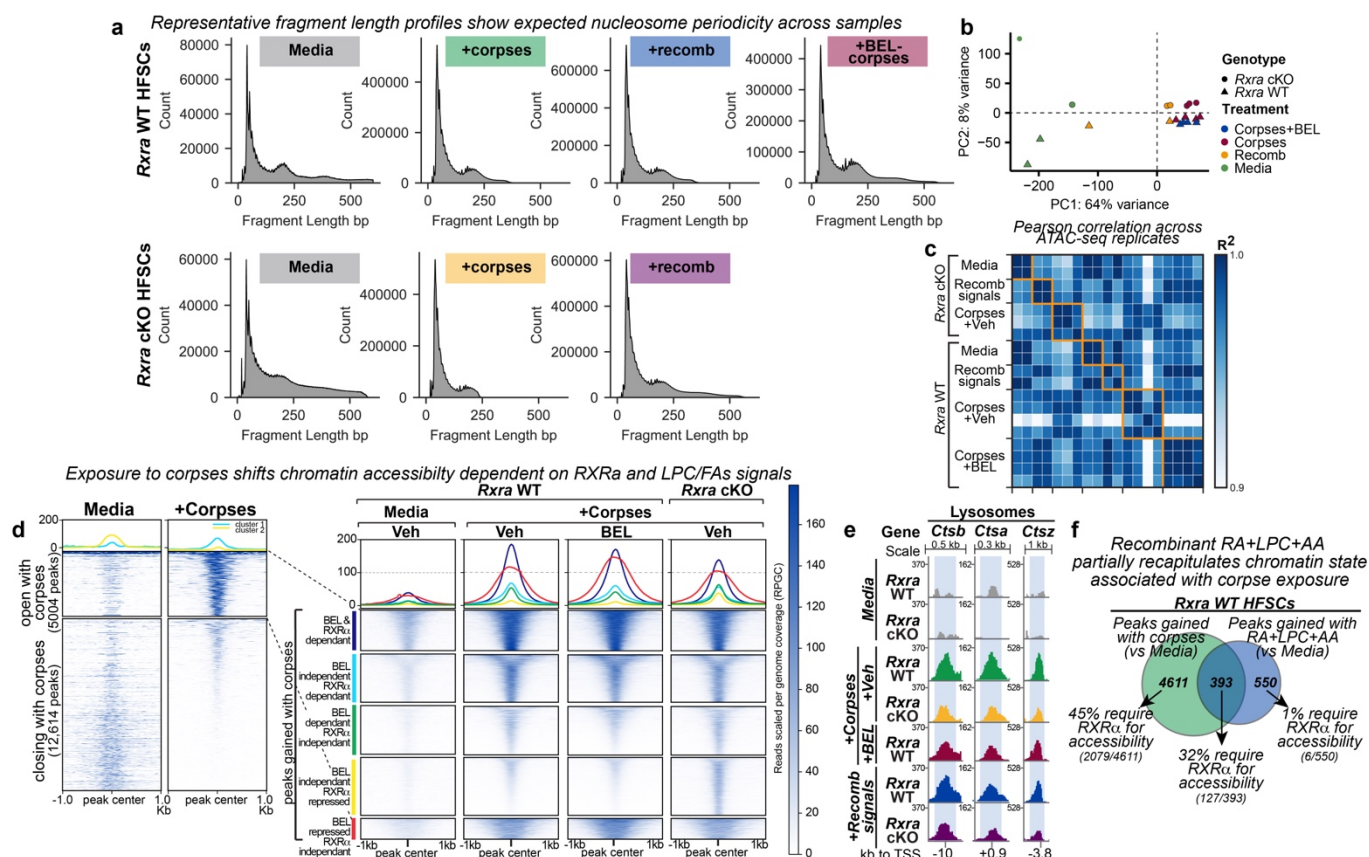
Extended Data Fig. 10 *(Related to Fig. 5)* **ATAC-seq shows differential accessibility in response to corpse-derived lysophosphatidylcholine and arachidonic acid dependent on RXRα. a,** Representative histograms of fragment lengths in base pairs (bp) detected for ATAC-seq replicates. recomb, 9-*cis* retinoic acid + all-*trans* retinoic acid + lysophosphatidylcholine + arachidonic acid; WT, wild type; cKO, conditional knockout. **b,** Principal component analysis on reads mapped to peaks. n=2 biological replicates per genotype per condition. **c,** Pearson correlation (R^2) values for reads mapped to peaks. **d,** Heatmap showing all peaks with significantly altered accessibility between *Rxra* WT and cKO replicates exposed to corpses with (+Veh, vehicle) or without (+BEL, bromoenol lactone) lysophosphatidylcholine + arachidonic acid. Signal for pooled replicate samples is in reads per genome coverage (RPGC) (colour bar legend, right). Each row corresponds to a detected peak, centered and extended +/- 1kb. Peaks are clustered based on differential accessibility relative to *Rxra* WT+Veh corpses, and summarized as the mean accessibility signal per region in a dark blue line (peaks that close in BEL and *Rxra* cKO), a light blue line (peaks that close in cKO only), a green line (peaks that close in BEL only), a yellow line (peaks that open in cKO only) or a red line (peaks that open in BEL only) in the graph at top. **e,** Replicate pooled peak tracks for enhancers associated with lysosomal genes. Annotated as in Fig. 5f. **f,** Venn diagram representation comparing peaks that open in response to corpses with those gained in response to retinoic acid (RA) + lysophosphatidylcholine (LPC) + arachidonic acid (AA) ('Recomb' condition) in *Rxra* WT HFSCs. Arrows indicate the percentage of peaks that require RXRα for accessibility within each category. Notably, enhancer peaks associated to phagocytic genes fall within the 32% of peaks gained in response to both corpses and recombinant signal that require *Rxra* for accessibility, which are shown in Fig. 5f.

References

1   Nagata, S. Apoptosis and Clearance of Apoptotic Cells. *Annu Rev Immunol* **36**, 489-517 (2018). https://doi.org:10.1146/annurev-immunol-042617-053010

2   Doran, A. C., Yurdagul, A., Jr. & Tabas, I. Efferocytosis in health and disease. *Nat Rev Immunol* **20**, 254-267 (2020). https://doi.org:10.1038/s41577-019-0240-6

3   Boada-Romero, E., Martinez, J., Heckmann, B. L. & Green, D. R. The clearance of dead cells by efferocytosis. *Nat Rev Mol Cell Biol* **21**, 398-414 (2020). https://doi.org:10.1038/s41580-020-0232-1

4   Medina, C. B. & Ravichandran, K. S. Do not let death do us part: 'find-me' signals in communication between dying cells and the phagocytes. *Cell Death Differ* **23**, 979-989 (2016). https://doi.org:10.1038/cdd.2016.13

5   Arandjelovic, S. & Ravichandran, K. S. Phagocytosis of apoptotic cells in homeostasis. *Nat Immunol* **16**, 907-917 (2015). https://doi.org:10.1038/ni.3253

6   Morioka, S., Maueroder, C. & Ravichandran, K. S. Living on the Edge: Efferocytosis at the Interface of Homeostasis and Pathology. *Immunity* **50**, 1149-1162 (2019). https://doi.org:10.1016/j.immuni.2019.04.018

7   Sachet, M., Liang, Y. Y. & Oehler, R. The immune response to secondary necrotic cells. *Apoptosis* **22**, 1189-1204 (2017). https://doi.org:10.1007/s10495-017-1413-z

8   Munoz, L. E., Lauber, K., Schiller, M., Manfredi, A. A. & Herrmann, M. The role of defective clearance of apoptotic cells in systemic autoimmunity. *Nat Rev Rheumatol* **6**, 280-289 (2010). https://doi.org:10.1038/nrrheum.2010.46

9   Kinchen, J. M. & Ravichandran, K. S. Phagosome maturation: going through the acid test. *Nature Reviews Molecular Cell Biology* **9**, 781-795 (2008). https://doi.org:10.1038/nrm2515

10   Hsu, Y. C., Pasolli, H. A. & Fuchs, E. Dynamics between stem cells, niche, and progeny in the hair follicle. *Cell* **144**, 92-105 (2011). https://doi.org:10.1016/j.cell.2010.11.049

11   Greco, V. *et al.* A two-step mechanism for stem cell activation during hair regeneration. *Cell Stem Cell* **4**, 155-169 (2009). https://doi.org:10.1016/j.stem.2008.12.009

12   Genander, M. *et al.* BMP signaling and its pSMAD1/5 target genes differentially regulate hair follicle stem cell lineages. *Cell Stem Cell* **15**, 619-633 (2014). https://doi.org:10.1016/j.stem.2014.09.009

13   Mesa, K. R. *et al.* Niche-induced cell death and epithelial phagocytosis regulate hair follicle stem cell pool. *Nature* **522**, 94-97 (2015). https://doi.org:10.1038/nature14306

14   Heitman, N. *et al.* Dermal sheath contraction powers stem cell niche relocation during hair cycle regression. *Science* **367**, 161-166 (2020). https://doi.org:10.1126/science.aax9131

15   Weedon, D. & Strutton, G. Apoptosis as the mechanism of the involution of hair follicles in catagen transformation. *Acta Derm Venereol* **61**, 335-339 (1981).

16   Wu, Y., Singh, S., Georgescu, M.-M. & Birge, R. B. A role for Mer tyrosine kinase in αvβ5 integrin-mediated phagocytosis of apoptotic cells. *Journal of Cell Science* **118**, 539-553 (2005). https://doi.org:10.1242/jcs.01632

17   Mangelsdorf, D. J. & Evans, R. M. The RXR heterodimers and orphan receptors. *Cell* **83**, 841-850 (1995). https://doi.org:10.1016/0092-8674(95)90200-7

18   Durand, B., Saunders, M., Leroy, P., Leid, M. & Chambon, P. All-trans and 9-cis retinoic acid induction of CRABPII transcription is mediated by RAR-RXR heterodimers bound to DR1 and DR2 repeated motifs. *Cell* **71**, 73-85 (1992). https://doi.org:10.1016/0092-8674(92)90267-g

19   Mangelsdorf, D. J. Vitamin A receptors. *Nutr Rev* **52**, S32-44 (1994). https://doi.org:10.1111/j.1753-4887.1994.tb01385.x

20   Ebisawa, M. *et al.* Retinoid X Receptor-Antagonistic Diazepinylbenzoic Acids. *Chemical and Pharmaceutical Bulletin* **47**, 1778-1786 (1999). https://doi.org:10.1248/cpb.47.1778

29

21   Mukundan, L. *et al.* PPAR-δ senses and orchestrates clearance of apoptotic cells to promote tolerance. *Nature Medicine* **15**, 1266-1272 (2009). https://doi.org:10.1038/nm.2048

22   A-Gonzalez, N. *et al.* Apoptotic Cells Promote Their Own Clearance and Immune Tolerance through Activation of the Nuclear Receptor LXR. *Immunity* **31**, 245-258 (2009). https://doi.org:10.1016/j.immuni.2009.06.018

23   Kiss, R. S., Elliott, M. R., Ma, Z., Marcel, Y. L. & Ravichandran, K. S. Apoptotic Cells Induce a Phosphatidylserine-Dependent Homeostatic Response from Phagocytes. *Current Biology* **16**, 2252-2258 (2006). https://doi.org:10.1016/j.cub.2006.09.043

24   Rőszer, T. *et al.* Autoimmune Kidney Disease and Impaired Engulfment of Apoptotic Cells in Mice with Macrophage Peroxisome Proliferator-Activated Receptor γ or Retinoid X Receptor α Deficiency. *The Journal of Immunology* **186**, 621-631 (2011). https://doi.org:10.4049/jimmunol.1002230

25   Hoijman, E. *et al.* Cooperative epithelial phagocytosis enables error correction in the early embryo. *Nature* **590**, 618-623 (2021). https://doi.org:10.1038/s41586-021-03200-3

26   Medina, C. B. *et al.* Metabolites released from apoptotic cells act as tissue messengers. *Nature* **580**, 130-135 (2020). https://doi.org:10.1038/s41586-020-2121-3

27   Lauber, K. *et al.* Apoptotic cells induce migration of phagocytes via caspase-3-mediated release of a lipid attraction signal. *Cell* **113**, 717-730 (2003). https://doi.org:10.1016/s0092-8674(03)00422-7

28   Gude, D. R. *et al.* Apoptosis induces expression of sphingosine kinase 1 to release sphingosine-1-phosphate as a "come-and-get-me" signal. *FASEB J* **22**, 2629-2638 (2008). https://doi.org:10.1096/fj.08-107169

29   Elliott, M. R. *et al.* Nucleotides released by apoptotic cells act as a find-me signal to promote phagocytic clearance. *Nature* **461**, 282-286 (2009). https://doi.org:10.1038/nature08296

30   Chekeni, F. B. *et al.* Pannexin 1 channels mediate 'find-me' signal release and membrane permeability during apoptosis. *Nature* **467**, 863-867 (2010). https://doi.org:10.1038/nature09413

31   Truman, L. A. *et al.* CX3CL1/fractalkine is released from apoptotic lymphocytes to stimulate macrophage chemotaxis. *Blood* **112**, 5026-5036 (2008). https://doi.org:10.1182/blood-2008-06-162404

32   Atsumi, G. *et al.* Distinct roles of two intracellular phospholipase A2s in fatty acid release in the cell death pathway. Proteolytic fragment of type IVA cytosolic phospholipase A2alpha inhibits stimulus-induced arachidonate release, whereas that of type VI Ca2+-independent phospholipase A2 augments spontaneous fatty acid release. *J Biol Chem* **275**, 18248-18258 (2000). https://doi.org:10.1074/jbc.M000271200

33   Peter, C. *et al.* Migration to apoptotic "find-me" signals is mediated via the phagocyte receptor G2A. *J Biol Chem* **283**, 5296-5305 (2008). https://doi.org:10.1074/jbc.M706586200

34   Peter, C. *et al.* Release of lysophospholipid 'find-me' signals during apoptosis requires the ATP-binding cassette transporter A1. *Autoimmunity* **45**, 568-573 (2012). https://doi.org:10.3109/08916934.2012.719947

35   Ravichandran, K. S. Find-me and eat-me signals in apoptotic cell clearance: progress and conundrums. *Journal of Experimental Medicine* **207**, 1807-1817 (2010). https://doi.org:10.1084/jem.20101157

36   Kim, S. J., Gershov, D., Ma, X., Brot, N. & Elkon, K. B. I-PLA(2) activation during apoptosis promotes the exposure of membrane lysophosphatidylcholine leading to binding by natural immunoglobulin M antibodies and complement activation. *J Exp Med* **196**, 655-665 (2002). https://doi.org:10.1084/jem.20020542

37   Calder, P. C. Dietary arachidonic acid: harmful, harmless or helpful? *British Journal of Nutrition* **98**, 451-453 (2007). https://doi.org:10.1017/s0007114507761779

38   Tallima, H. & El Ridi, R. Arachidonic acid: Physiological roles and potential health benefits - A review. *J Adv Res* **11**, 33-41 (2018). https://doi.org:10.1016/j.jare.2017.11.004

39   Lengqvist, J. *et al.* Polyunsaturated fatty acids including docosahexaenoic and arachidonic acid bind to the retinoid X receptor alpha ligand-binding domain. *Mol Cell Proteomics* **3**, 692-703 (2004). https://doi.org:10.1074/mcp.M400003-MCP200

40   de Urquiza, A. M. *et al.* Docosahexaenoic acid, a ligand for the retinoid X receptor in mouse brain. *Science* **290**, 2140-2144 (2000). https://doi.org:10.1126/science.290.5499.2140

41   Brash, A. R. Arachidonic acid as a bioactive molecule. *Journal of Clinical Investigation* **107**, 1339-1345 (2001). https://doi.org:10.1172/jci13210

42   Heyman, R. A. *et al.* 9-cis retinoic acid is a high affinity ligand for the retinoid X receptor. *Cell* **68**, 397-406 (1992). https://doi.org:10.1016/0092-8674(92)90479-v

43   Levin, A. A. *et al.* 9-cis retinoic acid stereoisomer binds and activates the nuclear receptor RXR alpha. *Nature* **355**, 359-361 (1992). https://doi.org:10.1038/355359a0

44   Giguere, V., Ong, E. S., Segui, P. & Evans, R. M. Identification of a receptor for the morphogen retinoic acid. *Nature* **330**, 624-629 (1987). https://doi.org:10.1038/330624a0

45   Petkovich, M., Brand, N. J., Krust, A. & Chambon, P. A human retinoic acid receptor which belongs to the family of nuclear receptors. *Nature* **330**, 444-450 (1987). https://doi.org:10.1038/330444a0

46   Foitzik, K. *et al.* Control of murine hair follicle regression (catagen) by TGF-β1*in vivo*. *The FASEB Journal* **14**, 752-760 (2000). https://doi.org:10.1096/fasebj.14.5.752

47   Fujino, N. *et al.* Sensing of apoptotic cells through Axl causes lung basal cell proliferation in inflammatory diseases. *J Exp Med* **216**, 2184-2201 (2019). https://doi.org:10.1084/jem.20171978

48   Juncadella, I. J. *et al.* Apoptotic cell clearance by bronchial epithelial cells critically influences airway inflammation. *Nature* **493**, 547-551 (2013). https://doi.org:10.1038/nature11714

49   Monks, J. *et al.* Epithelial cells as phagocytes: apoptotic epithelial cells are engulfed by mammary alveolar epithelial cells and repress inflammatory mediator release. *Cell Death & Differentiation* **12**, 107-114 (2005). https://doi.org:10.1038/sj.cdd.4401517

50   Shankman, L. S. *et al.* Efferocytosis by Paneth cells within the intestine. *Curr Biol* **31**, 2469-2476 e2465 (2021). https://doi.org:10.1016/j.cub.2021.03.055

51   Lee, C. S. *et al.* Boosting Apoptotic Cell Clearance by Colonic Epithelial Cells Attenuates Inflammation In Vivo. *Immunity* **44**, 807-820 (2016). https://doi.org:10.1016/j.immuni.2016.02.005

52   Park, D. *et al.* BAI1 is an engulfment receptor for apoptotic cells upstream of the ELMO/Dock180/Rac module. *Nature* **450**, 430-434 (2007). https://doi.org:10.1038/nature06329

53   Akhtar, N., Li, W., Mironov, A. & Charles. Rac1 Controls Both the Secretory Function of the Mammary Gland and Its Remodeling for Successive Gestations. *Developmental Cell* **38**, 522-535 (2016). https://doi.org:10.1016/j.devcel.2016.08.005

54   Ichimura, T. *et al.* Kidney injury molecule–1 is a phosphatidylserine receptor that confers a phagocytic phenotype on epithelial cells. *Journal of Clinical Investigation* **118**, 1657-1668 (2008). https://doi.org:10.1172/jci34487

Methods

The following previously generated mouse lines were used in this study: *Rxra^Flox* (ref.[55]; Jax stock 013086)*, Sox9CreER* (ref.[56])*, Krt14-rtTA* (ref.[57]; Jax stock 008099)*, Rosa26^lox-STOP-lox-YFP* (ref.[58]; Jax stock 006148; referred to as *R26^YFP*)*, Rosa26^mTmG* (ref.[59]; Jax stock 007576; referred to as *R26^mTmG*)*, Rosa26^Brainbow2.1* (ref. [60]; Jax stock 013731, referred to as *R26^Brainbow2.1*)*, Rosa26^lox-STOP-lox-Cas9-EGFP* (ref.[61]; Jax stock 026175, referred to as *R26^Cas9-EGFP*)*, Rosa26^lox-STOP-lox-DTA* (ref.[62]; Jax stock 010527, referred to as *R26^DTA*) and *Mertk^-/-* (full knockout, ref.[63]). The *Mertk* knockout mice used in this study are referred to as *Mertk^-/-V2* in the originating paper. Wild type CD1 or C57BL/6 animals were originally purchased from Charles River and The Jackson Laboratories, respectively, and maintained as in house colonies.

Mice were maintained and bred under specific-pathogen-free conditions at the Comparative Bioscience Center (CBC) at The Rockefeller University, an Association for Assessment and Accreditation of Laboratory Animal Care (AALAC)-accredited facility. *Mertk* knockout animals and C57BL/6J wild type controls (maintained as separate colonies) were bred and maintained in a specific-pathogen-free facility at Yale University. All animals were bred and maintained under a strict 12-hour light cycle and fed with standard chow. The temperature of the animal rooms was 20-26°C, and the humidity was 30-70%. Adult animals were housed in cage with a maximum of five mice. All mouse protocols were approved by the Institutional Animal Care and Use Committee (IACUC) at The Rockefeller University, or by the IACUC at Yale University.

For comparative assessments of phenotype between control and mutant animals, age and sex matched mice were used, with preference given to littermate controls wherever possible. For our inducible overexpression studies, a *Krt14-rtTA^+/-* (heterozygous) male was mated with CD1 females and all offspring were transduced with lentivirus at embryonic day (E) 9.5 (see following sections). Offspring of both genotypes received doxycycline by intraperitoneal (i.p.) injection (0.5mg/mouse) at postnatal day (P) 14 to activate *Krt14-rtTA* within 12hr, and expression was maintained by feeding the mother and pups doxycycline (2mg/kg) chow (Bioserv). *Krt14-rtTA^-* animals were used as control, with *Krt14rtTA^+* mice as the experimental group. To generate RXRa control and conditional knockout mice for experiments, the *RXRa^Flox* line was crossed with *Sox9CreER^+; R26^YFP* animals. *Sox9CreER^-* mice with any *Rxra^Flox;R26^YFP* genotype, and *Rxra^fl/+;Sox9CreER^+;R26-YFP^fl/+* mice were used as controls, while experimental mice were *Rxra^fl/fl;Sox9CreER^+;R26-YFP^fl/+*. All animals received tamoxifen (2% in corn oil) (Sigma-Aldrich) to activate *Sox9CreER,* administered by i.p. injection once a day for 3 days, as indicated. *Sox9CreER* was similarly activated when crossed to *R26^mTmG* (to label HFSCs prior to FACS-isolation and culture)*, R26^Brainbow2.1* (to stochastically label HFSCs and identify functional phagocytes), and *R26^Cas9-EGFP*(to mosaically knockout *Rxra*). To activate *Sox9CreER* sparsely when crossed to *R26^DTA*, 2% tamoxifen was i.p. injected once early in second telogen.

Hair cycle staging

Male and female mice have different hair cycle lengths due to a longer telogen quiescence phase in females, but otherwise progress through the hair cycle similarly. In addition to sex, strain and individuals

867 also affect hair cycle stages. Therefore, we always determine hair cycle stage by visual inspection, and
868 morphological staging on sectioned tissue. Specifically, for C57BL/6 pure and mixed backgrounds, visual
869 inspection was performed by trimming full-length telogen hairs with electric clippers to reveal dorsal skin.
870 Hair follicle (HF) entry into anagen was determined by darkening of skin and reappearance of hair. Catagen
871 progression was determined by lightening of the skin, which appears black at the end of anagen, to a near
872 complete loss of pigmentation (greyish-pink skin) by late catagen. Entry into telogen was marked by the
873 appearance of completely unpigmented (pink) skin. In unpigmented mice (CD1 strains), histological analysis
874 of HF morphology was used to confirm hair cycle staging based on relative age.

875 For all experiments, a small piece of midline dorsal skin was taken in parallel from each mouse, fixed
876 and processed for sectioning and immunofluorescence to precisely stage the hair cycle. Hair cycle was
877 staged based HF morphology[64-67], as well as by immunofluorescence for markers of anagen (EdU-
878 incorporation following a 2hr pulse chase), catagen (cleaved caspase-3 and/or TUNEL positivity) or telogen
879 (pSMAD1/5/9 and/or Lef1). For samples obtained from anagen or catagen stage mice the dorsal back skin
880 was subdivided in two along the anterior-posterior axis prior to the experiment, as precise hair cycle stage
881 differs anterior to posterior (with anterior generally one substage ahead). For anagen samples, 5'-ethynyl-
882 2'-deoxyuridine (EdU) was injected i.p. (50ug/g) (Sigma-Aldrich) and chased for 2hr prior to collection.

883

884 **Induction and knockout constructs**

885 *RXRα-induction:* To make TRE-RXRa-Myc; pGK-H2B-RFP, human *RXRa* cDNA was PCR-amplified
886 from pSV-Sport-RXRα (a gift from Bruce Spiegelman; Addgene #8882)[68], and a NheI site was introduced at
887 the 5'end. This was then inserted into the NheI and EcoRI restriction sites of a pLKO vector modified to
888 contain the inducible tetracycline response element at the 5' end, as well as a 3'-myc epitope tag. Prior to
889 packaging this construct as a lentivirus, induction of *RXRa* was tested in culture using FACS-isolated
890 *Krt14rtTA*[+] keratinocytes grown in E300 media. Briefly, cells were transiently transfected with the TRE-RXRα
891 construct using Effectene into keratinocytes in a 6-well plate format, following the manufacturer's protocol
892 (Invitrogen). 48 hrs later doxycycline (100ng/ml) was added to induce RXRα expression for a further 24 hrs.
893 Cells were fixed and stained for Myc-tag and RXRa, as described for cell culture immunofluorescence.

894 *RXRα-mosaic knockout:* To identify efficient CRISPR guide RNAs (sgRNA) against mouse *Rxra*, we
895 synthesized oligos targeting exon 4 with BsmBI restriction sites at 5' and 3' respectively (IDT). Oligos were
896 subcloned into pLentiGuide-Puro (a gift from Feng Zhang; Addgene #52963), following the Zhang lab
897 protocol[69]. To select a guide for *in vivo* use, we first tested the cutting efficiency in culture using *K14Cre*[+];
898 *R26*[Cas9-EGFP] expressing keratinocytes. pLentiGuide-Puro constructs were transiently transfected using
899 Effectene into keratinocytes in a 6-well plate format, following the manufacturer's protocol (Invitrogen). After
900 72 hrs, genomic DNA was harvested using QuickExtract DNA Extraction Solution (Lucigen), and gDNA was
901 prepared by heating to 65°C for 10 min followed by heat inactivation at 95°C for 2 min. Following PCR-
902 amplification of each guide target region, a T7 endonuclease I cutting assay (NEB) was used to identify the
903 extent of insertions/deletions for each guide. The most efficient guide showed ~70% genome editing events

904   *in vitro*, and was cloned with its U6 promoter into a modified pLKO vector containing a constitutive pGK-

905   driven mScarlet fluorophore (3' to the sgRNA) for lentiviral preparation.

906

907 **Lentiviral preparation and Injection**

908   High-titre lentivirus was prepared and embryonic day (E) 9.5 embryos of indicated genotypes were

909   infected with lentivirus delivered by ultrasound-guidance microinjection into the amniotic sac as previously

910   described[70,71]. At E9.5 the surface ectoderm exists as a single layer of unspecified skin progenitors, which

911   can be efficiently, selectively and stably transduced by the viral DNA, without transduction of dermal cell

912   types[71].

913

914 **HFSC culture**

915   All primary hair follicle stem cell (HFSC) lines were grown on a layer of mitomycin C-inactivated

916   3T3/J2 feeder fibroblast cells, and maintained in E intermediate (300uM) calcium media[72] supplemented with

917   10uM Y-27632 (Selleckchem) ("E300-Y media")[73]. The 3T3/J2 fibroblast cell line was expanded in

918   DMEM/F12 media (Thermo Fisher Scientific) with 10% CFS (Gibco), 100U/ml streptomycin and 100mg/ml

919   penicillin. Cells were grown at 37^oC, with 7.5% $CO2$, and media was routinely changed every 2-3 days. Cell

920   lines were grown to confluency, then propagated by digesting with 0.25% Trypsin EDTA (Gibco) for 5-10

921   min at 37^oC and resuspended with culture media for passaging. Experiments were conducted with cells at

922   passages 8-10. For experiments, cells were switched to E intermediate calcium media without Y-27632

923   ("E300 media") and cultured for 24-48hr prior to the experiment.

924   Primary HFSCs were derived from the following mouse crosses at second telogen: *R26-mTmG$^{fl/+}$;*

925   *Sox9CreER$^-$* (mTomato$^+$ HFSCs to make apoptotic corpses), *R26-mTmG$^{fl/+}$; Sox9CreER$^+$* (mGFP$^+$ HFSCs

926   to make naïve HFSC to expose to corpses), *Rxra$^{+/+}$; Sox9CreER$^+$; R26-YFP$^{fl/fl}$* (*Rxra* wild type YFP$^+$ HFSCs),

927   and *Rxra$^{fl/fl}$; Sox9CreER$^+$; R26-YFP$^{fl/fl}$* (*Rxra* conditional knockout YFP$^+$ HFSCs). All HFSCs were FACS-

928   isolated (described later) and cultured as described. To generate *Rxra* wild type and conditional knockout

929   HFSC lines, cells were FACS isolated, and cultures were established prior to activation of *Sox9CreER by* 4-

930   hydroxytamoxifen (4-OHT). At passage 2, *Sox9CreER* was activated in culture by 4-OHT in solution (Sigma

931   Aldrich); to do so it used at a final concentration of 1uM in E300-Y media to treat HFSCs. Media plus 4-OHT

932   was refreshed each day for three consecutive days, and then replaced by E300-Y. HFSCs were allowed to

933   grow for 4 further days prior to FACS isolation of YFP$^+$ cells.

934   To prepare corpses, fully confluent mTomato$^+$ HFSCs were treated with 200uM cisplatin (in 0.9%

935   saline) for 18hrs. Dead and dying cells were collected from the supernatant by pelleting at 700xg for 5 min,

936   washed once with E300 media, and returned to the plate in fresh E300 media. Prior to returning the floating

937   corpses, dying adherent cells were rinsed with PBS to remove residual cisplatin and a minimal amount of

938   fresh E300 media was added. Corpses were allowed to condition the media for a further 3-4hrs. Apoptotic

939   cell corpses were collected by tapping the side of the plate and pipetting their media over them to detach

940   dying cells. Floating and detached corpses were collected and pelleted by centrifugation as before. Corpse

34

941 conditioned media was carefully removed to a separate tube, before resuspending corpses in a minimal

942 volume of fresh E300 media. To label any corpses derived from 3T3/J2 fibroblasts, corpses were next

943 incubated with DiI-CM (Invitrogen) for 5 min at 37°C before pelleting and washing with PBS as before.

944 DiI/mTomato+ corpses were resuspended in their corpse conditioned media, counted and aliquoted (in their

945 conditioned media) directly onto experimental plates (media removed prior) at a ratio of roughly 10 corpses:1

946 HFSC. For corpse-conditioned media experiments, corpses were prepared as described and then spun out

947 of the media at 1200xg for 10 min. Corpse-conditioned media was further strained through a 0.45um syringe

948 filter, prior to use. Corpses and/or conditioned media were always prepared immediately prior to their use.

949 Manipulation of corpse-derived signals was achieved by adding small molecule inhibitors to the

950 corpses after the removal of cisplatin (16uM bromoenol lactone (Sigma Aldrich); 100nM MPA08) or by

951 incubating the corpses with recombinant molecules for 15-20 min prior to adding them to naïve HFSCs (1U

952 Apyrase; 1ng/ml AnnexinV). Vehicle treated control corpses were incubated with 1% DMSO. Similar

953 preparations were made for corpse-conditioned media. To manipulate corpse-sensing mechanisms on

954 HFSCs, naïve mGFP+ or YFP+ HFSCs were pretreated with the indicated antagonist (1nM UVI3003; 1uM

955 HX531; 1uM JTE013; 100nM BMS 777607; 1uM AGN 193109) (first four: Tocris Bioscience; last one: R&D

956 Systems) for 30 min prior to corpse or corpse-conditioned media addition. When adding corpses or

957 conditioned media, the concentration of antagonist was maintained by adding an additional amount of the

958 appropriate compound to the corpses and/or conditioned media.

959 To test the ability of recombinant molecules to recapitulate corpse secreted signals, mGFP+ or YFP+

960 HFSCs were cultured in E300 media plus the indicated concentrations of recombinant molecules (see figures

961 and figure legends). Molecules were prepared and stored as stock solutions according to manufacturer's

962 instructions. Briefly, 9-*cis* retinoic acid and all-*trans* retinoic acid (both R&D Systems) were each dissolved

963 in 100% DMSO, protected from light, and stored long term at -80°C with working solutions kept at -20°C.

964 Recombinant lysophosphatidylcholine, sphingosine-1-phosphate, and arachidonic acid (all Tocris

965 Bioscience) were each dissolved in 100% ethanol and stored like the retinoids. Free nucleotides were

966 purchased as 100mM stocks of dATP or dUTP as sodium salts in ultrapure water (NEB) and stored at -20°C.

967 Stock solutions were diluted individually or in combinations with E300 media for experiments.

968 In pilot experiments nuclear accumulation (by immunofluorescence) of RXRα or RARγ peaked at 30

969 min post corpse exposure, and so that time point was used to assess immediate effects of corpse-derived

970 signals or recombinant molecules in subsequent experiments. Similarly, the number of corpse-containing

971 HFSCs plateaued at 4-6 hrs after corpse addition, and so transcriptional activation of the phagocytic

972 program, surface expression of phagocytic receptors and corpse engulfment (latter two by FACS) were

973 routinely assessed at that time point.

974

975 **Intradermal injections**

976 Adult mice in early second catagen (CatII) were anesthetized using isoflurane prior to intradermal

977 injections. Isofluorane anesthetization was maintained throughout the procedure using a nose cone for

978   delivery. Back skin was shaved using electric clippers and the surface sterilized by wiping with ethanol wipes.

979   Vehicle or small molecule containing solutions were prepared by diluting appropriate chemical in sterile PBS

980   plus 1% FluoSpheres Carboxylate-modified microspheres (1.0um, Thermo Fisher Scientific #F8816) to

981   assess placement of the injection on tissue sections. To find the injection site for repeated intradermal

982   injections on subsequent days, a small dot was made with permanent marker which the needle was inserted

983   through. 1ml insulin syringes with the needle bent to approximately 45° were used to shallowly inject through

984   the epidermis to the dermal space approximately 3-5mm from the injection site. An injection volume of 25ul

985   was delivered per injection site, with an average of 4 injection sites per mouse: two anterior and two posterior.

986   Vehicle injections (10% DMSO) were randomly designated to either the left or right side, with the

987   contralateral skin receiving the indicated small molecules. Following the injections, mice were placed in their

988   home cage on a heating pad to recover. Compounds were prepared at 100X the cell culture working solution,

989   from the same stock solutions. To inhibit the phagocytic program across the course of catagen, intradermal

990   injections were performed three times, separated by 20-24hrs. Animals were sacrificed by lethal CO_2

991   administration, 4hrs after the final injection (at CatVII-VIII).

992

993   **Tissue collection and sectioning**

994   For immunofluorescence analysis of tissue sections, mice were shaved following lethal CO_2

995   administration and their back skin dissected. Back skin was stretched onto Whatman paper for stability, and

996   immediately prefixed in 1% or 4% paraformaldehyde (PFA) for 1 hr at 4°C or 30 min at 25°C, respectively.

997   After fixing, tissue was washed twice with PBS for 10 min at 4°C, before incubating in 30% sucrose in PBS

998   at 4°C overnight. Tissue was embedded in OCT medium (VWR) and frozen on dry ice blocks before storage

999   at -80°C. Alternatively, fresh frozen tissue was prepared without prefixation by directly embedding the skin

1000   in OCT after it was placed on whatman paper. Frozen tissue blocks were sectioned at 20um on a Leica

1001   cryostat and mounted on SuperFrost Plus slides (Thermo Fisher). When necessary, sections were stored at

1002   -20°C prior to use.

1003

1004   **Immunofluorescence**

1005   *Skin sections:* Following sectioning, tissue was allowed to dry on the slide for 1 hr in a partially closed

1006   slide box. Fresh frozen tissue was post-fixed with 4% PFA for 5 min, followed by washing in phosphate-

1007   buffered saline (PBS) three times for 5 min each. Pre-fixed tissue sections started with the PBS wash step

1008   to remove attached Whatman paper. Following washes, samples were permeabilized and blocked in

1009   blocking buffer (5% donkey serum, 2.5% fish gelatin, 1% BSA, 0.3% Triton in PBS) for 1 hr at room

1010   temperature. Primary antibodies were incubated overnight at 4°C, samples were washed for 5 min in PBS

1011   (three times) at room temperature, and secondary antibodies were incubated together with DAPI (to label

1012   nuclei) for 1 hr at room temperature. Following three final PBS washes of 5 min each, samples were mounted

1013   in Prolong Diamond Antifade Mountant (Invitrogen) for imaging. For TUNEL labelling, the Cell Death

1014   Detection Kit (TMR red or FITC; Roche) was used according to manufacturer's instructions, with application

1015 of secondary antibodies. A modification was made to halve the concentration of the substrate labelling

1016 component to reduce background fluorescence in the skin. Antibodies were used as follows: rabbit anti-

1017 cleaved-caspase-3 (Cell Signalling, 9661, 1:250), rat anti-RFP (Chromotek, 5F8, 1:1000), rabbit anti-RFP

1018 (MBL, PM005, 1:1000), chicken anti-GFP/YFP (Abcam, ab13970, 1:1000), goat anti-P-cadherin (R&D,

1019 AF761, 1:250), rabbit anti-keratin14 (Fuchs laboratory, 1:200), rabbit anti-myc epitope (71D10) (Cell

1020 Signalling, 2278, 1:250), rat biotinylated anti-CD45 (Biolegend, 5530, 1:200), rabbit anti-RXRα (D6H10) (Cell

1021 Signalling, 3085, 1:250), rabbit anti-RARγ (D3A4) (Cell Signaling, 8965, 1:250), rabbit anti-MFGE8

1022 (Invitrogen, PA5-109955, 1:200), rat AlexaFluor647-conjugated anti-F4/80 (BM8) (Biolegend, 123121,

1023 1:200), and rat biotinylated anti-Itga6/CD49f (GoH3) (Biolegend, 313603, 1:500). All secondary antibodies

1024 used were raised in a donkey host, and conjugated to AlexaFluor350, AlexaFluor488, Rhodamine,

1025 AlexaFluor568, or AlexaFluor647 (Jackson ImmunoResearch Laboratory; 1:500). 4',6-diamidino-2-

1026 phenylindole (DAPI) was used to label nuclei (1:10,000). To co-stain RARγ and RXRα, the rabbit primary

1027 antibodies were individually directly conjugated to one of AlexaFluor350, AlexaFluor488, AlexaFluor568, or

1028 AlexaFluor647 using the rabbit specific Zenon Antibody Labelling Kit (Thermo Fisher Scientific) and following

1029 manufacturer's instructions.

1030 *Cell culture:* For immunofluorescence experiments, feeders were split onto poly-L-lysine coated glass

1031 coverslips, seeded in 12-well plates 24 hrs prior to the addition of HFSCs. HFSCs were grown to confluency

1032 before feeders were detached by repeated PBS washes, and corpse or corpse conditioned media

1033 experiments were performed. At the end of the experiment, cells were washed twice with PBS and prefixed

1034 with 4% PFA for 3 min at 25°C. Cells were washed three times with PBS and stained as for tissue sections.

1035

Microscopy

1037 Images of *Sox9CreER; Rosa26$^{Brainbow2.1}$* tissue was acquired using a Zen-software driven Zeiss LSM

1038 780 inverted laser scanning confocal microscope and 20X air objective (NA=0.8), a 40X water immersion

1039 objective (NA=1.2), or a 63X oil immersion objective (NA=1.4). To separate CFP, YFP, GFP, RFP and

1040 AlexaFluor647 fluorophores, excitation with specific laser lines (405, 440, 488, 514, 561, 594, and 633) and

1041 narrow wavelength emission cut-offs on 4 detectors were set up as follows: CFP (ex.440nm, em.450nm-

1042 490nm), GFP (ex. 488nm, em. 500nm-515nm), YFP (ex. 514nm, em. 525nm-570nm), RFP (ex. 561nm, em.

1043 595nm-620nm), and AlexaFluor647 (ex. 633nm, em. 650nm-690nm). Due to their well-separated excitation

1044 and emission spectra, GFP and AlexaFluor647 were acquired simultaneously on the same detector. Stacks

1045 with a 1um step were acquired. Confocal microscopy was performed in The Rockefeller University's Bio-

1046 Imaging Resource Center, RRID:SCR_017791.

1047 Images of all other cryosections were acquired using a Zen-software driven Zeiss Axio Observer.Z1

1048 epifluorescent/brightfield microscope with a Hamamatsu ORCA-ER camera, Axiocam350, and an

1049 ApoTome.2 slider (to reduce light scatter in *z*). Stacks with a 1um step were acquired. Apotome acquired

1050 images were processed via "Apotome Raw Convert" function, and stitched (if necessary), in Zen software.

1051 Subsequent image processing was conducted in ImageJ. For presentation purposes, images were cropped

1052 and assembled in Adobe Illustrator.

1053

1054 **Electron microscopy**

1055 Dissected back skin was placed on thin paper towel for stability, and fixed in 2% glutaraldehyde, 4%

1056 PFA, and 2mM $CaCl_2$ in 0.1 M sodium cacodylate buffer (pH 7.2) for 2hr at room temperature, postfixed in

1057 1% osmium tetraoxide and processed for Epon embedding. Ultrathin sections of 60-65nm were

1058 counterstained with uranyl acetate and lead citrate, before images were taken with a transmission electron

1059 microscope (Tecnai G2-12;FEI) equipped with a digital camera (AMT BioSprint29). Samples were processed

1060 and imaged at The Rockefeller Electron Microscopy Resource Center.

1061

1062 **Flow cytometry**

1063 To obtain single-cell suspensions for fluorescence activated cell sorting (FACS) at all stages of the

1064 hair cycle, back skin was excised, and the dermal side scraped with a dull scalpel to remove excess fat prior

1065 to incubation with 0.25% collagenase (Sigma-Aldrich) in warm PBS, dermal side down for 45-60 min at 37^oC

1066 with gentle rotation in a plastic petri dish. The dermal side was scraped gently with a dull scalpel to

1067 mechanically dissociate cells in the lower outer root sheath (ORS) and hair bulb ("dermal fraction"). The

1068 dermal fraction was only kept for late anagen and early-mid catagen samples, and was processed separately

1069 from the epidermal fraction. To collect the epidermal fraction, the skin was placed dermal side down in 0.25%

1070 trypsin-EDTA (Gibco) for 20-25 min at 37^oC with gentle rotation. The hairy side of the skin was scraped

1071 against the direction of hair growth with a dull scalpel to release cells in the upper HF (including the HF bulge

1072 stem and hair germ progenitor cells). For both dermal and epidermal fractions, the resulting cell suspensions

1073 were pipetted up and down with a 5ml serological pipette for 5 minutes, before being quenched with FACS

1074 buffer (5% fetal bovine serum, FBS, in PBS). Plastic petri dishes were rinsed with 5ml of FACS buffer 2-3

1075 times, which was collected and added to the appropriate cell suspension. Suspensions were filtered through

1076 sequential 70um and 40 um nylon filters (VWR), before being pelleted at 350xg for 15 min at 4^oC. Cell pellets

1077 were resuspended in ice cold FACS buffer, re-filtered into FACS tubes, and incubated with primary

1078 antibodies for 20 min on ice. Secondary antibodies and LysoTracker DeepRed (Invitrogen, 1:4000) were

1079 added directly to FACS tubes, and incubation continued for 10 min on ice. Samples were further diluted with

1080 FACS buffer plus DNase (Roche) to minimize cell clumping prior to sorting or analysis. For analysis of RXRα

1081 levels by FACS, cells were stained with cell-surface specific primary and secondary antibodies, before being

1082 fixed and processed using the BD Cytofix/Cytoperm kit following manufacturer's instructions. Primary

1083 antibodies were used as follows: rat biotinylated anti-CD45 (30-F11) (eBioscience, Cat #13-0451-82, 1:200),

1084 rat biotinylated anti-CD117 (2B8) (eBioscience, 13-1171-82, 1:200), rat biotinylated anti-CD140a (APA5)

1085 (eBioscience, 13-1401-82, 1:200), rat biotinylated anti-CD31 (390) (eBioscience, 13-0311-82, 1:200), rat

1086 anti CD34-FITC (RAM34) (eBioscience, 11-0341-82, 1:200), rat anti CD34-eFluor660 (RAM34)

1087 (eBioscience, 50-0341-82,1:200), rat anti CD49f/Itga6-PercpCy5.5 (GoH3) (BioLegend, 313617, 1:250), rat

1088   anti-Ly6A/E(Sca1)-APC-Cy7(BioLegend, 108125, 1:1000), rabbit anti-RXRα (D6H10) (CST, 3085, 1:250),

1089   rat anti-Tyro3/Dtk-AlexaFluor700 (R&D Systems, FAB759N, 1:200), rat anti-Mertk-AlexaFluor700 (R&D

1090   Systems, FAB5912N, 1:200), and rat anti-Axl-AlexaFluor700 (R&D Systems, FAB8541N, 1:200). Secondary

1091   antibodies were used as follows: Strepavidin-PE-Cy7 (1:3000) and donkey AlexaFluor 488 or AlexaFluor568

1092   (1:500). AnnexinV-AlexaFluor568 (Invitrogen, A13202, 1:100) and/or DAPI was used to identify apoptotic

1093   and dying cells, respectively. For FACS using AnnexinV, primary and secondary antibody staining was

1094   performed in AnnexinV Binding Buffer (10mM HEPES, 140mM NaCl, 2.5mM $CaCl_2$, pH 7.4).

1095   For HFSC isolation for *in vitro* culture and bulk ATAC-sequencing, cells were sorted using a 70um

1096   nozzle into E300-Y media and FACS buffer. For bulk RNA-sequencing, cells were sorted using a 70um

1097   nozzle directly into Trizol and FACS buffer. For single cell RNA-sequencing cells were sorted with an 85um

1098   nozzle into 96-well PCR plates (Bio-Rad) containing 2ul of lysis buffer [0.2% Triton X-100, 2U/ul RNaseOUT

1099   (Thermo Scientific), 0.25uM oligo-dT30VN primer, 1:2x10^6 diluted ERCC spike-in RNAs (Ambion)]. Sorting

1100   was performed on a BD FACSAriaII equipped with Diva software (BD Biosciences).

1101   For FACS analysis, live cell suspensions from back skin were collected and analyzed in the same

1102   manner as for sorting. Alternatively, cultured HFSCs were trypsinized for 7-10min (as for passaging the cell

1103   lines), and pelleted at 300xg before resuspension, filtering and incubating with primary antibodies. A

1104   minimum of 20,000 HFSCs were analyzed per sample using either a BD LSRII Flow Cytometer or a BD

1105   Fortessa Flow Cytometer (BD Bioscience). For analysis of the Brainbow2.1 HFSCs, a LSRII specially

1106   equipped with a 445nm laser was used to excite CFP, separately from YFP/GFP and RFP.

1107   Flow cytometry was performed at The Rockefeller University's Flow Cytometry Resource Center,

1108   RRID:SCR_017694. Flow cytometry plots were generated using FlowJo to illustrate the strategies used for

1109   cell isolation, and manually compensated for presentation. Representative sort schemes pertaining to

1110   *Sox9CreER*; *R26^Brainbow2.1* analysis of functionally phagocytic HFSCs, wild-type isolation of HFSCs for single-

1111   cell RNAseq and ATACseq across the hair cycle, RXRα overexpression and knockout in HFSCs, and

1112   *Sox9CreER;R26^DTA* ectopic corpse response are available in Supplementary Information.

1113

1114   **scRNA-sequencing libraries**

1115   Single-cell RNA-sequencing libraries were prepared from FACS-isolated HF epithelial cells in AnaVI,

1116   CatVI, and CatVII, using a slightly modified Smart-Seq2 protocol as previously described[74,75]. For each hair

1117   cycle stage, cells from 3-6 animals were pooled prior to FACS-isolation. In brief, cells were sorted into

1118   hypotonic lysis buffer, snap frozen in liquid nitrogen and stored at -80°C until all samples were collected.

1119   Cells were lysed by heating at 72°C for 3 min, followed by reverse transcription of mRNA using dT30 oligos,

1120   template switching oligos and Maxima H- reverse transcriptase. The whole transcriptome was amplified (15

1121   cycles) by KAPA HiFi DNA polymerase (Roche), and then size-selected using 0.6X AmpPure XP beads

1122   (Beckman Coulter). To exclude cells with poor amplification, and wells containing multiple cells, qPCR for

1123   *Gapdh* was performed. Illumina sequencing libraries were indexed with unique 5' and 3' barcode

1124   combinations (up to 384 cells) using the Nextera XT DNA library preparation kit (Illumina). Libraries were

1125 pooled and size-selected with 0.9X AmpPure XP beads. Prior to sequencing on Illumina NextSeq500 using

1126 a 75 bp paired-end read mid-output setting, library quality was assessed by TapeStation (Agilent).

1127

1128 **ATAC-sequencing libraries**

1129 ATAC-seq was performed on 20,000-75,000 (*in vivo* samples) or 50,000 (culture samples) FACS-

1130 sorted HFSCs, as previously described[76-78]. Briefly, cells were lysed in ATAC lysis buffer for 1 min on ice,

1131 washed and nuclei resuspended in transposase buffer. Genomic DNA was transposed using Tn5

1132 transposase (Illumina) for 30 min at 37°C, at which point the reaction was halted. Samples were uniquely

1133 barcoded in batches of 10-12 (in vivo samples) or one batch of 27 (cultured HFSCs), using Buenrostro[76] or

1134 Nextera XT index kit v2 indices. Sequencing libraries were prepared according to manufacturer's instructions

1135 (Illumina). Libraries were sequenced to a depth of 50-100 million sequences, using paired-end runs on an

1136 Illumina Novaseq 6000 (at The Rockefeller University Genomics Resource Center).

1137

1138 **RNA isolation**

1139 Total RNA was isolated from FACS-isolated HFSCs using the Direct-zol RNA MicroPrep kit (Zymo

1140 Research) following manufacturer's instructions. The optional DNase I treatment was included in all sample

1141 preps, and RNA was eluted in DNase/RNase-free water. Quality and concentration of RNA samples were

1142 determined using an Agilent 2100 Bioanalyzer. All samples for sequencing had RNA integrity (RIN) numbers

1143 >8.5. RNA samples were used for RT-qPCR or bulk RNA-sequencing, as described.

1144

1145 **Bulk RNA-sequencing libraries**

1146 Comparable amounts of RNA per sample were used to prepare bulk RNA-sequencing libraries using

1147 Illumina Trueseq standard mRNA library kit (non-stranded, poly-A selection) following manufacturer's

1148 guidelines. Libraries were then uniquely barcoded, pooled and sequenced on an Illumina Novaseq 6000

1149 using single-end runs (at Weill Cornell Medical College's Genomic Core Facility).

1150

1151 **RT- qPCR**

1152 Equivalent amounts of RNA were reverse transcribed using SuperScript III Reverse Transcriptase

1153 (Thermo Fisher Scientific) following manufacturer's instructions. To normalize cDNA amount across

1154 samples, primers for *B2m* were used. cDNAs were mixed with gene specific primers and SYBR green PCR

1155 MasterMix (Sigma Aldrich) and run on an Applied Biosystems 7900HT Fast Real-Time PCR system.

1156

1157 **Single cell and bulk RNA-sequencing analysis**

1158 Trimmed FASTQ files were obtained from the Rockefeller University's Genome Resource Center

1159 (scRNA-sequencing) or from the Genomic Core Facility (Weill Cornell Medical College; bulk RNA-

1160 sequencing), and raw sequencing reads were aligned to the mouse reference genome (UCSC release

1161 mm39) using STAR (v2.6)[79]. The expression values of each gene were quantified as both raw counts and

1162 transcripts per million (TPM) using Salmon (v.1.4.0)[80], and compiled in R (v.3.6.1) using Tximport(v.1.12.3)[81].

1163 *Bulk RNA-sequencing:* For differential gene expression analysis in R, low detection genes (minimum

1164 average read count <10) were filtered before DESeq2 analysis (v.1.16.1)[82]. Differential expression modelling

1165 used a negative binomial distribution and Wald test. Genes were differentially expressed for log_2[fold-

1166 change]>|1| and adjusted *P*<0.05. Heatmaps and bar graphs illustrating differential gene expression were

1167 constructed in a Python environment (detailed in next paragraph).

1168 *scRNA-sequencing:* Analysis and visualization of the data were conducted in a Python environment

1169 built on Pandas (v.2.0.1), NumPy (v.1.24.2)[83], SciPy (v.1.10.1)[84], scikit-learn (v.1.2.0), SCANPY (v1.9.3)[85],

1170 AnnData (v0.9.1)[85], matplotlib (v3.7.1)[86] and seaborn[87] packages. Raw count and metadata matrices for

1171 1489 single outer root sheath cells across the hair cycle were loaded in SCANPY as an AnnData object.

1172 Single cell data was preprocessed to remove lowly detected genes (expressed in <75 cells) and cells with

1173 low complexity libraries (<2,000 genes detected). SCANPY was used to normalize counts per cell, and highly

1174 variable genes were detected. Prior to dimensionality reduction by principal component analysis (PCA), data

1175 was centered and scaled. PCA was performed on highly variable genes, with 100 components and the

1176 svd_solver using 'arpack' (SCANPY default setting). To construct a *k*-nearest neighbours graph on

1177 Euclidean distance, 41 principal components were used (which captured 25% of the variance in the data).

1178 Data was visualized using uniform manifold projection (UMAP) in SCANPY, and clustering was done using

1179 the Leiden algorithm (with a resolution setting of 0.5). Cluster resolution was chosen after iterating through

1180 resolution parameters from 0.1 to 0.75, as best capturing both hair follicle cycle stages and anatomic location

1181 (upper bulge region/upper ORS versus hair germ/upper-middle ORS versus lower ORS). Marker gene

1182 expression based on the literature[10-12,75] , together with the FACS markers each population was sorted on,

1183 was used to identify clusters. SCANPY was used to visualize selected marker genes in dot plots, or as

1184 normalized counts visualized on UMAPs.

1185 Differential gene expression based on cluster identity was used in DESeq2 to identify genes that

1186 varied as cells transitioned from late anagen growth phase to catagen. Differential expression was performed

1187 as described for bulk RNA-sequencing, with the modification of a threshold of 0.75 to construct Wald tests

1188 of significance. Gene set enrichment analysis (GSEA) on differentially expressed genes was performed

1189 using GSEA software (v.4.3.2)[88,89], and run with the MSigDB 2022 mouse database. Gene set terms with

1190 FDR<0.1 and showing high normalized enrichment scores in catagen cells were considered interesting. To

1191 construct gene set scores based on the GSEA identified terms the corresponding *Mus musculus* gene lists

1192 were obtained by Amigo2 through the Gene Ontology consortium. The SCANPY "tl.score_genes" function

1193 was used to compute the average expression of each gene set across single cells, and normalized to a

1194 randomly sampled reference set of genes[90,91]. The resulting gene set scores were colour coded on

1195 corresponding UMAP visualizations of the data.

1196

1197 **ATAC-sequencing analysis**

1198   Trimmed FASTQ files were obtained from the Rockefeller University's Genome Resource Center and

1199   aligned to the mouse reference genome (UCSC release mm39 using Burrows-Wheeler Aligner (BWA), using

1200   BWA-MEM with default parameters. The output .sam files were name-sorted and duplicate reads were

1201   marked and removed using SAMtools (v.1.17)[92]. Peaks were called on each replicate using MACS3 (v.3.0.0)

1202   using the callpeak command, BAMPE, and a mappable genome estimate of 1.87×10^9 (from the ENCODE

1203   pipeline). The fraction of reads in peaks was calculated using bedTools (v. 2.31.0)[93] and used to scale bigwig

1204   files equivalently in deepTools (v.2.0.0)[94]. Bigwig files were created from deduplicated, pooled replicate bam

1205   files using deepTools, and normalized as reads per genome coverage. Pooled replicate bigwig files were

1206   also used to calculate peak coverage matrices to plot heatmaps of centered differential peaks, extended by

1207   1 kb upstream and downstream. Differential peak analysis was done in DESeq2, using read count matrices

1208   across each individual replicate from concatenated, merged union peak sets from each replicate. These

1209   union peak sets were created separately for *in vivo* samples and *in vitro* samples. Differential analysis used

1210   negative binomial modelling, and Wald's test for significance. To assign peaks to nearest expressed gene,

1211   part of the Inferelator-prior (v.0.3.8)[95] package was used. Peaks were assigned to genes if they fell 50 kb

1212   upstream or 5 kb downstream of the gene body and were curated for expression using either scRNA-seq (in

1213   vivo samples) or bulk RNA-seq (in vitro samples). To make sure that all potential enhancers for genes related

1214   to the apoptotic cell clearance program were identified, any unassigned intergenic peaks within

1215   approximately 200kb of phagocytosis-related genes were manually curated. If no genes were expressed

1216   transcriptionally in the interval between phagocytic gene and unassigned intergenic peak, the intergenic

1217   peak was considered a potential enhancer for said gene. Peaks of interest were visualized using the

1218   integrated genome viewer (IGV) software (v.2.13.2), together with .bed files of differential peaks.

1219   Motif enrichment analysis for *in vivo* samples was performed in two ways: First, the MEME suite (v.

1220   5.5.2) package XSTREME in web browser format was used to search for motifs enriched in differential

1221   peaks, using as background the union set of all peaks detected, and the JASPAR 2022 vertebrate CORE

1222   transcription factor motif database, with lengths of 6-18bp specified. Both known and *de novo* enriched motifs

1223   were collapsed to clusters based on similarity and ranked based on adjusted p-value. Second, the

1224   transcription factor occupancy prediction by investigation of ATAC-seq signal (TOBIAS, v.0.14.0)[96]

1225   framework was used to perform chromatin footprinting analysis. Briefly, replicate-pooled bam files read

1226   coverage across the genome was calculated and corrected for Tn5 transposase cutting bias before footprint

1227   scores were calculated within the union set of called peaks. TOBIAS footprint scores were used to compute

1228   differential binding between anagen and catagen pooled replicates, or between *Rxra* WT and cKO pooled

1229   replicates. RXR-family catagen bound footprints were visualized in IGV by pooling each individual RXR-

1230   family member's bed footprint file.

1231

1232   **Statistics**

1233   All data from every experiment were included for analysis unless an error was detected via failed

1234   positive or negative controls; in that case the entire experiment was excluded from analysis. Measurements

1235 were taken from distinct samples, unless stated otherwise. Experiments were not blinded, given the lack of

1236 ambiguity in phenotypes observed and internal controls used.

1237   Statistical and graphical analyses were performed in Jupyter Notebooks, running a custom Python

1238 environment built as described in the single cell sequencing analysis section. Sample sizes, replicates and

1239 statistical tests used are indicated in each figure legend. Unless otherwise stated, unpaired two-tailed

1240 Student's t-tests with a 95% confidence interval were performed to test for pair-wise differences among the

1241 means. Data is visualized as box-and-whiskers plots, with the box representing the first to third quartiles of

1242 the data set, the median line inside the box, and the whiskers extending a maximum of 1.5 times the inter-

1243 quartile range. Observations that fall outside this range are plotted independently. For clarity, each

1244 observation in a data set is also visualized as a point overlaid on the box plot.

1245

Additional References

1247 55   Chen, J., Kubalak, S. W. & Chien, K. R. Ventricular muscle-restricted targeting of the RXRα gene
1248   reveals a non-cell-autonomous requirement in cardiac chamber morphogenesis. *Development* **125**,
1249   1943-1949 (1998). https://doi.org:10.1242/dev.125.10.1943

1250 56   Soeda, T. *et al.* Sox9-expressing precursors are the cellular origin of the cruciate ligament of the knee
1251   joint and the limb tendons. *genesis* **48**, 635-644 (2010). https://doi.org:10.1002/dvg.20667

1252 57   Nguyen, H., Rendl, M. & Fuchs, E. Tcf3 Governs Stem Cell Features and Represses Cell Fate
1253   Determination in Skin. *Cell* **127**, 171-183 (2006). https://doi.org:10.1016/j.cell.2006.07.036

1254 58   Srinivas, S. *et al. BMC Developmental Biology* **1**, 4 (2001). https://doi.org:10.1186/1471-213x-1-4

1255 59   Muzumdar, M. D., Tasic, B., Miyamichi, K., Li, L. & Luo, L. A global double-fluorescent Cre reporter
1256   mouse. *genesis* **45**, 593-605 (2007). https://doi.org:10.1002/dvg.20335

1257 60   Snippert, H. J. *et al.* Intestinal Crypt Homeostasis Results from Neutral Competition between
1258   Symmetrically Dividing Lgr5 Stem Cells. *Cell* **143**, 134-144 (2010).
1259   https://doi.org:10.1016/j.cell.2010.09.016

1260 61   Randall *et al.* CRISPR-Cas9 Knockin Mice for Genome Editing and Cancer Modeling. *Cell* **159**, 440-455
1261   (2014). https://doi.org:10.1016/j.cell.2014.09.014

1262 62   Wu, S., Wu, Y. & Capecchi, M. R. Motoneurons and oligodendrocytes are sequentially generated
1263   from neural stem cells but do not appear to share common lineage-restricted progenitors in vivo.
1264   *Development* **133**, 581-590 (2006). https://doi.org:10.1242/dev.02236

1265 63   Akalu, Y. T. *et al.* Tissue-specific modifier alleles determine Mertk loss-of-function traits. *eLife* **11**
1266   (2022). https://doi.org:10.7554/elife.80530

1267 64   Parakkal, P. F. Morphogenesis of the hair follicle during catagen. *Z Zellforsch Mikrosk Anat* **107**, 174-
1268   186 (1970). https://doi.org:10.1007/BF00335223

1269 65   Lindner, G. *et al.* Analysis of apoptosis during hair follicle regression (catagen). *Am J Pathol* **151**,
1270   1601-1617 (1997).

1271 66   Magerl, M. *et al.* Patterns of proliferation and apoptosis during murine hair follicle morphogenesis.
1272   *J Invest Dermatol* **116**, 947-955 (2001). https://doi.org:10.1046/j.0022-202x.2001.01368.x

1273 67   Müller-Röver, S. *et al.* A Comprehensive Guide for the Accurate Classification of Murine Hair Follicles
1274   in Distinct Hair Cycle Stages. *Journal of Investigative Dermatology* **117**, 3-15 (2001).
1275   https://doi.org:10.1046/j.0022-202x.2001.01377.x

1276 68   Tontonoz, P., Hu, E., Graves, R. A., Budavari, A. I. & Spiegelman, B. M. mPPAR gamma 2: tissue-
1277   specific regulator of an adipocyte enhancer. *Genes & Development* **8**, 1224-1234 (1994).
1278   https://doi.org:10.1101/gad.8.10.1224

1279   69   Sanjana, N. E., Shalem, O. & Zhang, F. Improved vectors and genome-wide libraries for CRISPR
1280   screening. *Nature Methods* **11**, 783-784 (2014). https://doi.org:10.1038/nmeth.3047

1281   70   Beronja, S., Livshits, G., Williams, S. & Fuchs, E. Rapid functional dissection of genetic networks via
1282   tissue-specific transduction and RNAi in mouse embryos. *Nature Medicine* **16**, 821-827 (2010).
1283   https://doi.org:10.1038/nm.2167

1284   71   Beronja, S. & Fuchs, E.   351-361 (Humana Press, 2013).

1285   72   Rheinwald, J. G. & Green, H. Epidermal growth factor and the multiplication of cultured human
1286   epidermal keratinocytes. *Nature* **265**, 421-424 (1977). https://doi.org:10.1038/265421a0

1287   73   Yuan, S. *et al.* Ras drives malignancy through stem cell crosstalk with the microenvironment. *Nature*
1288   **612**, 555-563 (2022). https://doi.org:10.1038/s41586-022-05475-6

1289   74   Picelli, S. *et al.* Full-length RNA-seq from single cells using Smart-seq2. *Nature Protocols* **9**, 171-181
1290   (2014). https://doi.org:10.1038/nprot.2014.006

1291   75   Yang, H., Adam, R. C., Ge, Y., Hua, Z. L. & Fuchs, E. Epithelial-Mesenchymal Micro-niches Govern
1292   Stem Cell Lineage Choices. *Cell* **169**, 483-496.e413 (2017). https://doi.org:10.1016/j.cell.2017.03.038

1293   76   Buenrostro, J. D., Giresi, P. G., Zaba, L. C., Chang, H. Y. & Greenleaf, W. J. Transposition of native
1294   chromatin for fast and sensitive epigenomic profiling of open chromatin, DNA-binding proteins and
1295   nucleosome position. *Nature Methods* **10**, 1213-1218 (2013). https://doi.org:10.1038/nmeth.2688

1296   77   Buenrostro, J. D., Wu, B., Chang, H. Y. & Greenleaf, W. J. ATAC-seq: A Method for Assaying Chromatin
1297   Accessibility Genome-Wide. *Current Protocols in Molecular Biology* **109** (2015).
1298   https://doi.org:10.1002/0471142727.mb2129s109

1299   78   Infarinato, N. R. *et al.* BMP signaling: at the gate between activated melanocyte stem cells and
1300   differentiation. *Genes & Development* **34**, 1713-1734 (2020).
1301   https://doi.org:10.1101/gad.340281.120

1302   79   Dobin, A. *et al.* STAR: ultrafast universal RNA-seq aligner. *Bioinformatics* **29**, 15-21 (2013).
1303   https://doi.org:10.1093/bioinformatics/bts635

1304   80   Patro, R., Duggal, G., Love, M. I., Irizarry, R. A. & Kingsford, C. Salmon provides fast and bias-aware
1305   quantification of transcript expression. *Nat Methods* **14**, 417-419 (2017).
1306   https://doi.org:10.1038/nmeth.4197

1307   81   Soneson, C., Love, M. I. & Robinson, M. D. Differential analyses for RNA-seq: transcript-level
1308   estimates improve gene-level inferences. *F1000Res* **4**, 1521 (2015).
1309   https://doi.org:10.12688/f1000research.7563.2

1310   82   Love, M. I., Huber, W. & Anders, S. Moderated estimation of fold change and dispersion for RNA-seq
1311   data with DESeq2. *Genome Biol* **15**, 550 (2014). https://doi.org:10.1186/s13059-014-0550-8

1312   83   Harris, C. R. *et al.* Array programming with NumPy. *Nature* **585**, 357-362 (2020).
1313   https://doi.org:10.1038/s41586-020-2649-2

1314   84   Virtanen, P. *et al.* SciPy 1.0: fundamental algorithms for scientific computing in Python. *Nat Methods*
1315   **17**, 261-272 (2020). https://doi.org:10.1038/s41592-019-0686-2

1316   85   Wolf, F. A., Angerer, P. & Theis, F. J. SCANPY: large-scale single-cell gene expression data analysis.
1317   *Genome Biol* **19**, 15 (2018). https://doi.org:10.1186/s13059-017-1382-0

1318   86   Hunter, J. D. Matplotlib: A 2D Graphics Environment. *Computing in Science & Engineering* **9**, 90-
1319   95 (2007). https://doi.org:10.1109/mcse.2007.55

1320   87   Waskom, M. seaborn: statistical data visualization. *Journal of Open Source Software* **6**, 3021 (2021).
1321   https://doi.org:10.21105/joss.03021

1322   88   Subramanian, A. *et al.* Gene set enrichment analysis: A knowledge-based approach for interpreting
1323   genome-wide expression profiles. *Proceedings of the National Academy of Sciences* **102**, 15545-
1324   15550 (2005). https://doi.org:10.1073/pnas.0506580102

89   Mootha, V. K. *et al.* PGC-1α-responsive genes involved in oxidative phosphorylation are coordinately downregulated in human diabetes. *Nature Genetics* **34**, 267-273 (2003). https://doi.org:10.1038/ng1180

90   Satija, R., Farrell, J. A., Gennert, D., Schier, A. F. & Regev, A. Spatial reconstruction of single-cell gene expression data. *Nature Biotechnology* **33**, 495-502 (2015). https://doi.org:10.1038/nbt.3192

91   Tirosh, I. *et al.* Dissecting the multicellular ecosystem of metastatic melanoma by single-cell RNA-seq. *Science* **352**, 189-196 (2016). https://doi.org:10.1126/science.aad0501

92   Li, H. *et al.* The Sequence Alignment/Map format and SAMtools. *Bioinformatics* **25**, 2078-2079 (2009). https://doi.org:10.1093/bioinformatics/btp352

93   Quinlan, A. R. & Hall, I. M. BEDTools: a flexible suite of utilities for comparing genomic features. *Bioinformatics* **26**, 841-842 (2010). https://doi.org:10.1093/bioinformatics/btq033

94   Ramirez, F. *et al.* deepTools2: a next generation web server for deep-sequencing data analysis. *Nucleic Acids Res* **44**, W160-165 (2016). https://doi.org:10.1093/nar/gkw257

95   Skok Gibbs, C. *et al.* High-performance single-cell gene regulatory network inference at scale: the Inferelator 3.0. *Bioinformatics* **38**, 2519-2528 (2022). https://doi.org:10.1093/bioinformatics/btac117

96   Bentsen, M. *et al.* ATAC-seq footprinting unravels kinetics of transcription factor binding during zygotic genome activation. *Nature Communications* **11** (2020). https://doi.org:10.1038/s41467-020-18035-1

Acknowledgements

Author contributions

K.S.S. and E.F. conceptualized the study, designed the experiments, interpreted the data, and wrote the paper. K.S.S. performed all experiments, with assistance from K.A.G, S.Y., M.T.T., A.B., Y.Y., N.I., and C.C. K.A.G, S.Y., M.T.T., and A.B. assisted with FACS experiments. K.A.G, S.Y., Y.Y., and N.I. prepared ATAC-seq libraries for sequencing. M.T.T. and A.B. collected skin samples for *Rxra* cKO-related experiments. K.S.S analyzed ATAC-seq data with input from Y.Y. K.A.G performed WT HFSC bulk RNA-seq. C.C. prepared RNA for bulk RNA-sequencing. J.M.L. performed all lentiviral injections. H.A.P. performed electron microscopy and interpreted images. C.V.R and S.G. contributed *Mertk* mice, and expertise. All authors provided input on the final manuscript.

Competing Interest

E.F. has served on the scientific advisory boards of L'Oreal and Arsenal Biosciences. C.V.R is a senior editor for eLife. S.G. has received grant support from Mirati Therapeutics. The other authors declare no competing interests.

Data availability

All data supporting the findings of this study are available within the Article and its Supplementary Information. All single-cell and bulk sequencing data generated within this study have been deposited at the Gene Expression Omnibus (GEO) under accession code GSE230523.

Code availability

Custom code for scRNA-seq and ATAC-seq for this study will be deposited at Zenodo. All other codes are available from the corresponding author on reasonable request.

Supplementary Information

Supplementary information is available for this paper.

Correspondence and requests for materials should be addressed to Elaine Fuchs (fuchslb@rockefeller.edu).